Optical Characterisation of Southern Ocean Phytoplankton

Frieda Morrison[1,2]

A Thesis presented for the Degree of
Master of Science

Supervisors: Dr. Sandy Thomalla[1]
Dr. Lisl Robertson Lain[1]
Prof. Marcello Vichi[2]

[1]Council for Scientific and Industrial Research (CSIR)

[2]Department of Oceanography
University of Cape Town (UCT)

July 2022

Abstract

Retrieving the optical properties of Southern Ocean (SO) phytoplankton with high confidence is critical to understanding the role of the Biological Carbon Pump (BCP). Satellite-based ocean colour remote sensing radiometry is the only observational capability that can provide synoptic views of upper ocean phytoplankton characteristics, at high spatial and temporal resolution of approximately 1 km globally, and a daily temporal resolution over a period of years to decades, as is required for climate studies. In many cases, these are the primary systematic observations available for chronically under-sampled marine systems such as the SO. Inversion algorithms are applied to satellite radiometry with the goal of characterising the optical properties of the in-water constituents, primarily phytoplankton. If the relationship between Inherent Optical Properties (IOPs) and biophysical phytoplankton assemblage characteristics, in terms of abundance, cell size and pigment composition, is well understood, biogeochemical information can be inferred from satellite-derived phytoplankton IOPs. This approach has greatly augmented global comprehension of climate change and the carbon cycle. The SO is typified by unique phytoplankton optical properties, distinct from those elsewhere in the world. Most notably among these is displaying characteristically "depressed" phytoplankton absorption spectra. It is understood that there are two main drivers behind this: unusually large cell sizes, and elevated pigment density resulting from physiological changes in response to the often low light environment (photoacclimation). The primary aim of this study is to investigate the observed seasonal variability in measured *in situ* SO IOPs, in conjunction with the UCT-CSIR[1] Equivalent Algal Populations (EAP) model of phytoplankton optical properties, to better understand the causal drivers of the optical differentiation of SO phytoplankton absorption. The EAP model is used to illustrate the biophysical source of the observed unique absorption characteristics, showing that the flattening of the spectra is driven primarily by photophysiological changes occurring during photoacclimation, namely increased density of intracellular chlorophyll *a*. The satellite-derived OC-CCI[2] phytoplankton absorption product, observed to reproduce elevated spectra more typical of other oceans, is investigated to determine this. The model is then used to simulate biophysically consistent phytoplankton backscatter, in order to investigate whether photoacclimation, resulting in the distinctive absorption properties of the SO, has any impact on phytoplankton backscatter and the magnitude of its contribution to the bulk water-leaving signal. A reduction in phytoplankton backscatter signal was demonstrated by the model. Discussion was made in the context of opportunities for the detection of constituent IOP retrievals and biogeochemical parameters from satellites in space.

[1] University of Cape Town & Council for Scientific and Industrial Research, South Africa
[2] Ocean Colour - Climate Change Initiative

Declaration

The work in this thesis is based on research carried out at UCT, the Department of Oceanography, South Africa and CSIR, South Africa. No part of this thesis has been submitted elsewhere for any other degree or qualification and it is all my own work unless referenced to the contrary in the text.

Acknowledgements

I would like to thank my supervisors Dr. Sandy Thomalla, Dr. Lisl Robertson-Lain, Prof. Marcello Vichi and Dr. Stewart Bernard for their technical advice and guidance.

I am grateful for the opportunity to have attended the Ocean Colour Data in Climate Studies training course in Plymouth, UK (September 2017) and the International Ocean-Colour Coordinating Group (IOCCG) Summer lecture series at the Observatoire Océanologique de Villefranche-sur-Mer, France (July 2018).

Thank you to all my colleagues and fellow students for the time spent together.

I would like to thank the staff and crew of the SA Agulhas II. I am thankful for the opportunity to have gone twice to Antarctica during my studies, and I hope the scientific contributions can be used for years to come.

Thank you to the Council for Scientific and Industrial Research (CSIR) / Southern Ocean Carbon and Climate Observatory (SOCCO) / National Research Foundation (NRF) for their financial support throughout my studies.

A special thanks to my parents for the interest they have embedded in me in the ocean and mathematics, and the most interest in my research throughout all the topic changes. Thank you to all my family and friends, and my dear friend for singing me guitar songs in exchange for my flute songs during the pandemic.

A special thanks to my husband who was willing to travel with me to Antarctica to collect data for the studies, and for his interest in my programming skills and enjoying my 3D plots. Also for all the laughs, because when life gets too serious, laughter is just the best medicine.

Table of Contents

Abstract 1
Declaration 3
Acknowledgements 4

Table of Notation 6

List of Figures 7

Chapter 1 10

1. Introduction and Literature Review 10
1.1. The Biological Carbon Pump 10
1.2. Inherent Optical Properties of Seawater 13
1.2.1. Phytoplankton Contribution 14
1.2.2. Non-Algal Component 14
1.3. Problem Description: The Unique Characteristics of Southern Ocean Phytoplankton IOPs 16
1.4. Aims and Objectives 17

Chapter 2 19

2. Experimental Methods 19
2.1 Equivalent Algal Populations Model of Phytoplankton IOPs 19
2.1.1. EAP Model Structure 19
2.1.2. Considerations for use of the EAP in the Southern Ocean 20
2.2. In situ Measurements 23
2.2.1. Data Collection 23
2.2.2. Chlorophyll a 23
2.2.3. Particulate Absorption 24
2.2.4. Particle Size Distributions (PSDs) 24
2.3 Satellite Data 26

Chapter 3 28

3. Results and Observations 28
3.1 Addressing Aim 1: Identifying the Drivers of the Observed Flattened Absorption Spectra in the Southern Ocean 28
3.1.1. Summer 29
3.1.2. Winter 31

3.1.3. Understanding the Drivers of Spectral Flattening: Pigment Packaging versus the Package Effect 34
3.1.4. Investigating the Satellite OC-CCI $a^{\Phi}(\lambda)$ Product 37
3.2. Addressing Aim 2: The Impact of Photoacclimation on Phytoplankton Backscatter 49
3.3. Addressing Aim 3: Implications for Carbon Estimates from Satellite 53
3.3.1. Pursuing Phytoplankton Carbon from $b_{bp}(\lambda)$ 54
3.3.2. Pursuing POC from Particulate Size Distributions 55
3.3.3. Careful Considerations Towards Parameterisation of a New C_{phyto} Approach 57

Chapter 4 58

4. Conclusions and Recommendations 59

5. References 61

6. Appendix 71
6.1. Supplementary Figures 71

Table of Notation

Symbol	Definition	Units
c_i	Chlorophyll *a* density per cell volume	kg m^{-3}
$R_{rs}(\lambda)$	Remote sensing reflectance	sr^{-1}
$a(\lambda)$	absorption coefficient	m^{-1}
$b(\lambda)$	scattering coefficient	m^{-1}
$c(\lambda)$	attenuation coefficient	m^{-1}
$b_b(\lambda)$	backscattering coefficient	m^{-1}
$a_\Phi(\lambda)$	phytoplankton absorption coefficient	m^{-1}
$a^*_\Phi(\lambda)$	chlorophyll-specific absorption coefficient	m^2/mg
$b_{b\Phi}(\lambda)$	phytoplankton backscattering coefficient	m^{-1}
$b^*_{b\Phi}(\lambda)$	chlorophyll-specific backscattering coefficient	m^2/mg
$b_{bp}(\lambda)$	total particulate backscattering	m^{-1}
$a_{NAP}(\lambda)$	absorption of depigmented (non-algal) particles	m^{-1}
$b_{bNAP}(\lambda)$	backscattering of depigmented (non-algal) particles	m^{-1}

List of Figures

Figure 1: Depicts the stations sampled on the SCALE a) Winter, b) Summer Leg 1 and c) Summer Leg 2 cruises. The colour of the dots reflect ambient [chl a*].*

Figure 2: Summer measurements for a) in situ $a_\Phi(\lambda)$ compared to b) EAP model $a_\Phi(\lambda)$ spectra. c) depicts the mean and standard deviation of the measured $a_\Phi(\lambda)$, while d) depicts the mean and standard deviation of the modelled $a_\Phi(\lambda)$ for the same stations. e) presents measured $a^*_\Phi(\lambda)$ compared to f) EAP modelled $a^*_\Phi(\lambda)$ for the same stations. All EAP modelled spectra for summer are generated with a c_i of 5 kg m^{-3}.

Figure 3: a) Winter measured $a_\Phi(\lambda)$ b) Winter modelled $a_\Phi(\lambda)$ using a c_i of 5 kg m^{-3}.

Figure 4: Winter (a) in situ *measured $a_\Phi(\lambda)$ spectra that are compared to (b) EAP model derived $a_\Phi(\lambda)$ spectra (c) mean and the standard deviation of the measured $a_\Phi(\lambda)$ (d) mean and the standard deviation of the modelled $a_\Phi(\lambda)$ (e) measured $a^*_\Phi(\lambda)$, and (f) EAP modelled $a^*_\Phi(\lambda)$ derived for phytoplankton of D_{effs} of 3 and 4 µm. All EAP modelled spectra for winter are generated with a c_i of 12 kg m^{-3}.*

Figure 5: Modelled $a^*_\Phi(\lambda)$ with (a) c_i of 12 kg m^{-3}, and variable D_{eff} and (b) D_{eff} of 5 µm with variable c_i (in kg m^{-3}).

Figure 6: Measured summer $a^*_\Phi(\lambda)$ (mean and standard deviation, in orange) plotted with modelled $a^*_\Phi(\lambda)$ with a c_i of 2 kg m^{-3} representing a favourable growth environment for a D_{eff} of 6 µm (green) and 12 µm (red) (as per the range of measured D_{eff}). Modelled $a^*_\Phi(\lambda)$ with a D_{eff} of 30 µm (blue) is the best fit to the measured data.

Figure 7: Measured winter $a^*_\Phi(\lambda)$ (mean and standard deviation, in orange) plotted with modelled $a^*_\Phi(\lambda)$ with a c_i of 2 kg m^{-3} representing a favourable growth environment for a D_{eff} of 3 µm (green) and 4 µm (red) (as per the range of measured D_{eff}). Modelled $a^*_\Phi(\lambda)$ with a D_{eff} of 30 µm (blue) is the best fit to the measured data.

Figure 8: Summer a) OC-CCI satellite derived $a_\Phi(\lambda)$ spectra compared to b) in situ measured $a_\Phi(\lambda)$ spectra. Mean and standard deviation of the c) OC-CCI satellite derived $a_\Phi(\lambda)$ spectra compared to d) in situ measured $a_\Phi(\lambda)$ spectra. The comparisons of satellite derived and measured $a_\Phi(\lambda)$ spectra using only the 2 matchups in time and location are depicted in e) station 6 and f) station 70.

Figure 9: Summer a) satellite $a^*_\Phi(\lambda)$ using satellite OC1 and OC5 algorithm derived [Chl a], b) in situ measured $a^*_\Phi(\lambda)$, c) mean and standard deviation of $a^*_\Phi(\lambda)$ using the satellite OC1 and OC5 algorithm derived [Chl a] and d) mean and standard deviation of the in situ measured $a^*_\Phi(\lambda)$.

Figure 10: Summer comparison of in situ measured [chl a] versus OC1 and OC5 satellite derived [chl a], with the final bar representing the average of all match up stations.

Figure 11: Summer a) satellite $a^*_\Phi(\lambda)$ using measured in situ [Chl a], b) in situ measured $a^*_\Phi(\lambda)$, c) mean and standard deviation of $a^*_\Phi(\lambda)$ using the in situ measured [Chl a] and d) mean and standard deviation of the in situ measured $a^*_\Phi(\lambda)$.

Figure 12: Summer a) satellite derived $a^*_\Phi(\lambda)$ for the matchups stations 6 and 70 using OC1 and OC5 algorithm derived [chl a] and b) using in situ measured $a^*_\Phi(\lambda)$ compared to c) in situ measured $a^*_\Phi(\lambda)$.

Figure 13: Winter a) OC-CCI satellite derived $a_\Phi(\lambda)$ spectra compared to b) in situ measured $a_\Phi(\lambda)$ spectra. Mean and standard deviation of the c) OC-CCI satellite derived $a_\Phi(\lambda)$ spectra compared to d) in situ measured $a_\Phi(\lambda)$ spectra.

Figure 14: Winter a) satellite $a^*_\Phi(\lambda)$ using satellite OC1 and OC5 algorithm derived [Chl a], b) in situ measured $a^*_\Phi(\lambda)$, c) mean and standard deviation of $a^*_\Phi(\lambda)$ using the satellite OC1 and OC5 algorithm derived [Chl a] and d) mean and standard deviation of the in situ measured $a^*_\Phi(\lambda)$.

Figure 15: *Winter comparison of in situ measured [chl a] versus OC1 and OC5 satellite derived [chl a], with the final bar representing the average of all match up stations.*

Figure 16: *Winter a) satellite $a^*_\Phi(\lambda)$ using measured in situ [Chl a], b) in situ measured $a^*_\Phi(\lambda)$, c) mean and standard deviation of $a^*_\Phi(\lambda)$ using the in situ measured [Chl a] and d) mean and standard deviation of the in situ measured $a^*_\Phi(\lambda)$.*

Figure 17: Winter a) OC-CCI satellite derived $a^*_\Phi(\lambda)$ spectra, b) OC-CCI satellite derived $a^*_\Phi(\lambda)$ normalised with in situ measured [chl a] compared to c) modelled $a^*_\Phi(\lambda)$ spectra using a c_i of 12.

Figure 18: Figure 7a) from Bricaud et al., (1995) depicting $a^*_\Phi(\lambda)$ for different values of [chl a] concentration between 0.03 to 10 mg m^{-3}.

Figure 19: Summer satellite total $b_{bp}(\lambda)$, compared to the corresponding modelled $b_{\square\square}(\lambda)$ for the same stations, including the proportional contribution of $b_{\square\square}(\lambda)$ to total $b_{bp}(\lambda)$, calculated as difference in averages.

Figure 20: Winter satellite total $b_{bp}(\lambda)$, compared to the corresponding modelled $b_{\square\square}(\lambda)$ for the same stations, including the proportional contribution of $b_{\square\square}(\lambda)$ to total $b_{bp}(\lambda)$, calculated as differences in averages.

Figure 21: Modelled phytoplankton $b^*_{b\Phi}(\lambda)$ with a constant D_{eff} (6 μm) but a changing c_i ranging from 2 to 12 kg m^{-3}.

Figure 22: An example of high biomass bloom conditions from the lower latitude Benguela upwelling system showing a) the in situ measured absorption (blue), the satellite $a_\Phi(\lambda)$ (orange) and the modelled $a_\Phi(\lambda)$ from in situ [chl a] of 43 mg m^{-3} (green) and b) the total satellite derived $b_{bp}(\lambda)$ (blue) and the modelled $b_{b\Phi}(\lambda)$ from in situ [chl a] of 43 mg m^{-3} (orange).

Figure 23: a) An example of low biomass conditions from the lower latitude Benguela upwelling system showing a) the in situ measured absorption (blue), the satellite $a_\Phi(\lambda)$ (orange) and the modelled $a_\Phi(\lambda)$ from in situ [chl a] of 1.4 mg m^{-3} (green) and b) the total satellite derived $b_{bp}(\lambda)$ (blue) and the modelled $b_{b\Phi}(\lambda)$ from the in situ [chl a] of 1.4 mg m^{-3} (orange).

Figure 24: Modelled $b^*_{b\Phi}(\lambda)$ for D_{eff} of 3 µm and 6 µm, with variable c_i of 2, 5 and 12 kg m^{-3}.

Supplementary Figure S1: Measured a) $a_\Phi(\lambda)$ spectra and b) $a^*_\Phi(\lambda)$ for all stations including the 8 negative spectra that were subsequently removed from the data set.

Supplementary Figure S2: Winter: all measured a) $a_\Phi(\lambda)$ spectra b) and $a^*_\Phi(\lambda)$ spectra.

Supplementary Figure S3: Four stations displaying the high $a_\Phi(\lambda)$ in the blue wavelength region characteristic of incomplete phytoplankton pigment extraction.

Supplementary Figure S4: Membership water class for summer.

Supplementary Figure S5: Membership water class for winter.

Chapter 1

1. Introduction and Literature Review

1.1. The Biological Carbon Pump

The Biological Carbon Pump (BCP) is an important contributor to the Southern Ocean (SO) carbon dioxide (CO_2) sink removing an estimated amount of 3 Pg of Carbon (C) from surface waters south of 30°S each year (33 % of the global organic C flux, Schlitzer 2002). The SO's BCP is also important for its role in regulating the supply of nutrients to thermocline waters. During photosynthesis, phytoplankton fix CO_2 as organic C which is subsequently transferred to the deep ocean in particulate and dissolved form when phytoplankton die and sink (Dall'Olmo *et al*., 2011). This process reduces the partial pressure gradient of CO_2 in the upper ocean, facilitating the absorption of CO_2 from the atmosphere and potentially reducing the impacts of anthropogenically driven climate change (Sarmiento *et al*., 2002). Further to this biological process, the process called the solubility pump shows that the surface-water carbon dioxide partial pressure (pCO_2) is further affected by CO_2 solubility that is indicated by seawater temperature and salinity (Dai *et al.*, 2022). These processes occur continuously, but at variable rates and scales from the minute (phytoplankton carbon fixation) to global scales (the carbon-climate pump), and over the entire depth of the ocean. Understanding these processes is critical for properly understanding the mechanisms of global climate change and being able to predict or forecast future climate and ecosystem impacts.

Phytoplankton community structure is influenced by changes in the light environment and nutrient supply, and is therefore variable across oceanic regions and different seasons. Further differences in phytoplankton community composition are driven by top-down controls from the grazing community (Finkel *et al*., 2010). One anticipated impact of climate change is an alteration of the nutrient and light supply to different oceanic environments (e.g. Winder *et al*., 2012), which could impact phytoplankton community structure and cell size. This would impact the amount of C and other elements in particulate matter and how much of it is exported to depth (Finkel *et al*., 2010). Thus, climate change driven alterations in community structure could alter the efficiency of the BCP (Le Quéré *et al*., 2007; Matear and Hirst, 1999). As such, being able to characterise phytoplankton community structure is of importance in the trajectory of ecosystem understanding (Chisholm *et al*., 1992; Finkel *et al*., 2010; Munk *et al*., 1952; Parsons *et al*., 1973; Semina 1972) .

Phytoplankton diversity is vast, and different species or types that fulfill similar ecological roles are often considered together under the term Phytoplankton Functional Types (PFTs) (IOCCG, 2014). PFTs are a useful concept since the food web structure, biogeochemical cycling of C and growth rates, are constrained by the elemental stoichiometry and cell size of phytoplankton (Finkel *et al*., 2010). One particularly pragmatic functional type delineation is that of cell size. Phytoplankton cell size encompasses a scope of nine orders of magnitude (Finkel *et al*., 2010), and is of fundamental ecological importance, notably for the role played in driving the BCP due to the relationship between particle size and sinking rates (Bienfang *et al*., 1984, Stemmann *et al*., 2012). A comprehensive guide to the identification of PFTs from space is found in the IOCCG PFT report (2014).

In situ data on phytoplankton community structure and cell size generates information for a very limited time and location, providing snapshots of an intricate system of biogeochemical and biophysical processes that are occurring continuously over much larger spatial and temporal scales. *In situ* measurements of phytoplankton community structure, carbon content and other biogeochemical parameters are simply impossible to acquire at the time and space scales necessary for investigating the impacts of climate change on ocean ecosystems. Satellite-based remote sensing radiometry (i.e. ocean colour) is the only observational capability that can provide synoptic views of upper ocean phytoplankton characteristics at high spatial and temporal resolution of approximately 1 km globally, and a daily temporal resolution over a period of years to decades that are required for climate studies. In many cases, these are the only systematic observations available for chronically under-sampled marine systems such as the SO. However, the enormous amount of data provided by satellite radiometry and differing algorithms for the retrieval of optical and biogeochemical quantities present considerable complexity for the accurate interpretation of these measurements. Moreover, current ocean colour algorithms tend not to incorporate the bio-optical properties of the SO and thus tend to perform poorly in this region (Kahru *et al*., 2010). This is likely due to their parameterisation with low-latitude bio-optical data sets whose properties differ from those of the SO. Optical modelling is an essential tool for observing and understanding the biogeochemical relationships and bio-optical interactions which result in the radiometric water-leaving signal that is measured by ocean colour remote sensing instruments. Satellite data, when interpreted using the insight provided by bio-optical models, can be applied to ocean biogeochemistry data and models towards a better understanding of the characteristics of the temporal and spatial distribution of phytoplankton community structure, primary production (PP) and carbon export. In this way, the role of the SO's BCP can also be better understood.

Satellite sensors measure the combined radiometric signal of water-leaving radiance and atmospheric irradiance, the former comprising not only the optical absorption and (back)scattering of both algal and non-algal particle assemblages, but also those of dissolved in-water constituents such as Coloured Dissolved Organic Matter (CDOM), whose concentration in the open ocean is closely related to the production of phytoplankton waste products (Kirk, 1994). Although the age of satellite oceanography has facilitated measurements of water-leaving radiometric signals, understanding and interpreting the relationship between in-water constituent composition (and variability) and their optical contribution to the ocean surface waters observable by satellite sensors is not straightforward. By investigating these relationships through bio-optical measurements and modelling, the strength and efficacy of the ocean BCP, its sensitivity to changes in earth's climate and ultimately the prediction of the long term changes in the global carbon cycle can be better understood (e.g., Cox *et al*., 2000; Orr *et al*., 2005).

1.2. Inherent Optical Properties of Seawater

The colour of the ocean continues to fascinate us. Light entering the ocean can either be absorbed or scattered by seawater constituents or by the seawater itself. Each seawater constituent (algal and non-algal particulate, and dissolved substances) has unique optical properties which are driven by their physical and chemical characteristics. These fundamental properties are known as Inherent Optical Properties (IOPs).

The IOPs of seawater and each of its constituents include the absorption coefficient, $a(\lambda)$, and the scattering coefficient, $b(\lambda)$, which together result in attenuation, $c(\lambda)$ (Morel 1974). Absorption is when light that is interacting with a suspension of particles, or with the water itself, is transformed into other forms of energy (Gibson *et al*., 2007). Absorbed light energy can be converted to heat, or in the case of phytoplankton into chemical energy via photosynthesis. Scattering occurs when light is deviated from a straight trajectory due to non-uniformities in the medium, with backscattering, $b_b(\lambda)$, being that portion of scattering which occurs in the backward direction (90° to 180°). $b_b(\lambda)$ is of particular interest in the context of satellite remote sensing as it determines the portion of incident light that is returned to the surface as an observable water-leaving signal. In other words, Remote Sensing Reflectance (R_{rs}) is a quantity retrievable from satellite measurements and is proportional to $b_b(\lambda)/(a(\lambda)+b_b(\lambda))$, (Vaillancourt *et al*., 2004). There is a reduction in the intensity of light as it travels through a medium, due to absorption or scattering, and this is called attenuation (Mobley 1994). IOPs are by definition independent of illumination conditions. It should be noted that R_{rs} and attenuation are apparent optical properties (AOPs) / quasi-AOPs (https://oceanopticsbook.info/view/inherent-and-apparent-optical-properties/introduction), and dependent on illumination.

In the SO the particle field is driven by its biological components (Talley, L.D. *et al*., 2011), with particle types that vary in concentration and composition over both time and location, with subsequent variability in their optical properties. Total backscatter comprising that of water itself, phytoplankton and non-algal particulates, including viral and bacterial particles, can be denoted as $b_{bTOT}(\lambda)$. Particulate backscatter, $b_{bp}(\lambda)$, is closely related to the bulk particle size distribution (Kostadinov *et al*., 2009; Neukermans *et al*., 2012; Ulloa *et al*., 1994). Knowledge of the relative abundance and optical contributions of different particle types is thus important for interpreting optical data (e.g. satellite radiometry) towards understanding the different roles they play in ocean ecosystems and the biogeochemical cycle. It is important to be able to accurately quantify phytoplankton IOPs, particularly their absorption, $a_\Phi(\lambda)$, and backscatter, $b_{b\Phi}(\lambda)$, so that phytoplankton information can be derived from the water-leaving signal. Distinguishing $b_{b\Phi}(\lambda)$, from non-algal particle abundance (and/or describing covariant relationships between them) is a topical area of

research (D'all Olmo *et al*., 2009; Organelli *et al*., 2020) and this capability is critical to identifying the phytoplankton assemblage characteristics essential for examining their role in the BCP.

1.2.1. Phytoplankton Contribution

The optical characteristics of phytoplankton assemblages are well understood to be driven by particle abundance, cell size, morphology and pigment characteristics (e.g. Laiolo *et al*., 2021). Variability in the magnitude of the phytoplankton-driven optical signal is understood to be largely driven by particle abundance and size (Bricaud *et al*., 2004; Kostadinov *et al*., 2009; Lain *et al*., 2014). Phytoplankton vary widely in their size as well as in their biophysical and biogeochemical constitution, and consequently their interaction with the underwater light field in terms of their absorption and scattering characteristics (Mobley, 1994). The primary drivers of variability in $a_{\Phi}(\lambda)$ are pigment quantity and type (Bricaud *et al*., 1988). Spectral $b_{b\Phi}(\lambda)$ also varies among phytoplankton types, driven primarily by particle size with some variability resulting from differences in the constitution of phytoplankton cell walls (Baird *et al*., 2022). For example, hard-shelled coccolithophores have a particularly high $b_{b\Phi}(\lambda)$, making them easily identifiable from space (Kopelevich *et al*., 2014). Coccolithophores have external plates of calcium carbonate that make the ocean appear milky white or turquoise during immense blooms.

There are many other cellular and community characteristics that also influence phytoplankton assemblage IOPs. These include morphology (shape) and ultrastructure (Bricaud *et al*., 1988). Alterations in phytoplankton physiology in response to environmental stressors can also affect the optical characteristics of IOPs. For example, photoacclimation in response to light availability can impact cellular density, which would subsequently impact the IOP signature (Graff *et al*., 2016; Behrenfeld *et al*., 2003). However, photoacclimation responses require sufficient iron to occur effectively (Moore *et al*., 2007) and since the SO is known to be severely limited by the micronutrient iron, particularly during the summer following biological uptake (Hassler *et al*., 2012), the degree of photoacclimation will likely vary both regionally and seasonally depending on iron supply and availability.

1.2.2. Non-Algal Component

Non-algal in-water constituents comprise both soluble and insoluble material. Insoluble (particulate) contributors to the non-algal optical signal may include colloids, bacteria, biogenic detritus, minerogenic particles of both biogenic (e.g., calcite liths and shells) and terrestrial origin (e.g. clays and sand), bubbles, micrograzers and viruses, suspended sediments and pollutants such as plastics (Bellacicco *et al*., 2019, Sosik, 2008). Non-algal

particulate absorption is denoted $a_{NAP}(\lambda)$, and is frequently approximated using an exponential slope (maximum in the blue, decreasing in the red) at a magnitude covarying with phytoplankton biomass (Morel 1988). Dissolved non-algal substances are referred to collectively as CDOM (also called gelbstoff). This is primarily a phytoplankton waste product that absorbs light in a manner that decreases exponentially with wavelength from a maximum in the ultraviolet. This allows for CDOM absorption to be described by two parameters, absorption at a reference wavelength $a_g(\lambda)$, and a slope parameter (S).

Although the composition and abundance of non-algal particles generates a significant source of variability in $b_b(\lambda)$ (Bellacicco *et al*., 2019), these attributes nonetheless remain very poorly characterised (Koestner *et al*., 2019). Non-algal backscatter $b_{bNAP}(\lambda)$ is frequently approximated using a simple wavelength-dependent relationship, with assumptions of some covariance between algal and non-algal particle concentrations. However, a recent study based on data from the South Atlantic concludes that there is no simple observable relationship between $b_{b\Phi}(\lambda)$ and $b_{bNAP}(\lambda)$ (Organelli *et al*., 2020). Small-sized (<2 μm), primarily organic particles appear to be the most important contributors to total particulate backscattering $b_{bp}(\lambda)$ under non-bloom conditions (Stamski *et al*., 2004). This is due to their high abundance relative to other particle types. Part of the reason for the poor optical characterisation of the non-algal particle composition is primarily due to the fact that data are not readily available. Only a few studies, such as Bellacicco *et al*., (2019), have investigated particulate assemblage composition in terms of the proportion of detrital particles covarying with phytoplankton biomass (as determined by [chl *a*]) versus the proportion that does not covary, and implications for observed variability in $b_{bp}(\lambda)$ in different oceanic regions. They concluded that in the SO, the portion of $b_{bNAP}(\lambda)$ that does not co-vary with [chl *a*] is a large fraction of $b_{bp}(\lambda)$ with respect to that of other oceans (Bellacicco *et al*., 2019).

1.3. Problem Description: The Unique Characteristics of Southern Ocean Phytoplankton IOPs

Szeto *et al*., (2011) describe the differing optical characteristics of the world's oceans, driven by variations in the in-water constituents described in Section 1.2. These regional differences in optical properties are intrinsically related to differences in ecological and biogeochemical processes (Szeto *et al*., 2011). The bio-optical relationships between [chl *a*] and water-leaving radiances differ between higher and lower latitudes (Dierssen and Smith 2000, Garcia *et al*. 2005, Mitchell and Holm-Hansen 1991, Mitchell and Kahru 2009). The SO is typified by unique phytoplankton optical properties, distinct from those elsewhere in the world, displaying characteristically "depressed" spectral chl *a*-specific (chl-specific) absorption, $a^*_\Phi(\lambda)$, (Robinson *et al*., 2021). The study by Robinson *et al*., (2021) concludes that this characteristic is due to (a possible combination of) lower concentrations of accessory pigments per unit chl *a*, and/or larger sized phytoplankton at lower [chl *a*] than are typically observed in other oceans.

Lower concentrations of accessory pigments per unit chl *a* than is observed elsewhere could be a characteristic that is unique to SO phytoplankton. However, this could also imply that fewer cells are needed to constitute a unit of chl *a*, revealing a higher concentration of chl *a* pigment in each cell. Such an increase in intracellular chl *a* density (c_i) is a typical phytoplankton photophysiological response to low light levels (photoacclimation) (Bellacicco *et al*., 2016, Halsey *et al*., 2015), a potential source of optical variability only mentioned in passing by Robinson *et al*., (2021). That study favours the size-related explanation and concludes that the observed depression in SO $a^*_\Phi(\lambda)$ is due in large part to the substantial contribution of microphytoplankton (>20 μm) to total biomass despite low [chl *a*].

In addition to differences in $a^*_\Phi(\lambda)$, it has also been observed that $b_{bNAP}(\lambda)$ in the SO can be very high (Bellacicco *et al*., 2018), suggesting that the detrital contribution to $b_{b\Phi}(\lambda)$ may be elevated. Given the paucity of *in situ* $b_{b\Phi}(\lambda)$ measurements in the SO, it is unknown whether the biophysical source of the depressed $a^*_\Phi(\lambda)$ should also affect $b_{b\Phi}(\lambda)$.

The implication of these observations is that satellite ocean colour inversion algorithms and other methods for retrieving constituent optical properties from remote sensing data may not perform well in the SO without acknowledgment and accommodation of these optical disparities. It should not be assumed that algorithms parameterised with lower-latitude bio-optical data sets from more temperate waters are applicable in this extreme Austral environment.

1.4. Aims and Objectives

The variability observed in measured *in situ* SO IOP's will be investigated in conjunction with the UCT-CSIR Equivalent Algal Populations (EAP) model of phytoplankton optical properties to better understand the causal drivers of the optical differentiation of SO $a^*_{\Phi}(\lambda)$ with respect to that of phytoplankton elsewhere. The model, when appropriately parameterised with *in situ* measurements, can investigate the biophysical source of their unique absorption characteristics, and can simulate biophysically consistent chl-specific backscatter, $b^*_{b\Phi}(\lambda)$, in order to address the questions at hand: Firstly, given the distinctive absorption properties of SO phytoplankton, what does this imply about potentially distinctive backscatter? Secondly, does this impact upon the magnitude of the phytoplankton contribution to the bulk water-leaving signal, and hence impact on the potential detection of such signal in the constituent IOP retrievals from space?

Bio-optical measurements made during the SO SCALE winter and summer cruises in 2019/2020 (see Methods) will be used in combination with the EAP model to address the following three key aims:

1. To identify the dominant driver/s of the observed flattened $a^*_{\Phi}(\lambda)$ as described by Robinson *et al*., (2021), in terms of pigment density and/or cell size.
2. To determine whether the driver/s of the observed impact on $a^*_{\Phi}(\lambda)$ have a corresponding impact on $b^*_{b\Phi}(\lambda)$.
3. To identify consequent implications for the derivation of the proportional contribution of phytoplankton carbon (C_{phyto}) to particulate organic carbon (POC) from satellite data.

This is a critical investigation towards being able to retrieve the magnitude of the phytoplankton contribution to satellite-measured bulk particulate backscatter $b_{bp}(\lambda)$. It is known that not all non-algal particles co-vary with phytoplankton abundance (Bellacicco *et al*., 2019), and that assumptions of covariability can lead to significant errors in POC estimations (Sathyendranath *et al*., 2017).

These three aims will be pursued by the fulfilment of the following three objectives:

a) Parameterising the EAP model for use in the Southern Ocean

The EAP model described in Section 2.1 has been used widely in coastal and inland waters of South Africa, but has yet to be employed in the open ocean waters of the SO, where phytoplankton communities are substantially different in terms of biomass, assemblage

size distribution, pigment composition and physiology. The first step towards using the model in this study is to parameterise it appropriately by constraining the input variables wherever possible using existing *in situ* measurements. This process is described further in Section 2.1.

b) Using the EAP model and satellite $a_{\Phi}(\lambda)$ data to investigate potential sources of observed variability in *in situ* SO $a_{\Phi}(\lambda)$ measurements

The EAP model input parameters will reflect measured *in situ* [chl *a*] and measured particle size distributions, represented in the model using an assemblage effective diameter (D_{eff}) (Bernard *et al*., 2007). A 'best fit' forward modelling approach is used to identify the potential range of input parameters with large uncertainty: particularly for that of the c_i, for which there is no corresponding measurement.

It should be emphasised that optical closure is not the goal of this undertaking. The aim is rather to investigate from a causal perspective the contrasting effects on the optics of D_{eff} and c_i in order to better understand the observed optical uniqueness of SO phytoplankton with respect to other oceans.

The *in situ* measured $a_{\Phi}(\lambda)$ and $a^*_{\Phi}(\lambda)$ is compared to the corresponding EAP model generated spectra.

The Ocean Colour Climate Change Initiative (OC-CCI) $a_{\Phi}(\lambda)$ and $a^*_{\Phi}(\lambda)$ data products coinciding with *in situ* measurement stations are then compared against the corresponding measured *in situ* $a_{\Phi}(\lambda)$ and $a^*_{\Phi}(\lambda)$ in order to evaluate the QAA algorithm retrieval of these quantities in the SO.

c) Use the model to simulate corresponding biophysically consistent $b^*_{b\Phi}(\lambda)$ and evaluate the potential for isolating $b_{b\Phi}(\lambda)$ from a bulk observation

With an appropriately parameterised representation of SO $a^*_{\Phi}(\lambda)$, with its identified drivers incorporated into the EAP model, the corresponding $b^*_{b\Phi}(\lambda)$ can be simulated using measurements of assemblage effective diameter and chlorophyll concentration (as was done for absorption). The satellite-derived $b_{bp}(\lambda)$ (reflecting total backscatter from phytoplankton and non-algal particulates) are compared with the EAP modelled $b_{b\Phi}(\lambda)$ to determine the proportional contribution of phytoplankton to $b_{bp}(\lambda)$ in summer (sufficient light) versus in winter (typically light limited).

Chapter 2

2. Experimental Methods

2.1 Equivalent Algal Populations Model of Phytoplankton IOPs

2.1.1. EAP Model Structure

The UCT-CSIR EAP model is a physics-based semi-analytical phytoplankton IOP model that allows investigation into the causal mechanisms inducing optical variability in phytoplankton assemblages.

It is based on a spherical two-layered geometry (Bernard *et al*., 2009) and built from biophysical first principles, presenting the opportunity to investigate the causal impact of changes in phytoplankton community structure and physiology (in terms of [chl *a*], D_{eff} and c_i) on the optical properties. The outer sphere represents the phytoplankton chloroplast (20 % of the total particle volume) and is characterised by the spectral imaginary refractive index chosen for the dominant light-harvesting pigments of a selected phytoplankton assemblage. The pigmented material, which is chl *a* in the largest part, is strongly absorbing. The outer sphere is also highly refractive and its real refractive index drives the backscatter. The inner sphere is approximately represented as the phytoplankton cytoplasm, which contains about 80 % water, is almost colourless and is weakly absorbing (Stephens 1995; Zaneveld and Kitchen, 1995). IOPs are computed at high spectral resolution between 400 and 900 nm at the interval specified. The interval specified in the model for this study is 5 nm.

There are two unique and fundamental features of the EAP model: Firstly, the $a_{\Phi}(\lambda)$ is constrained by the maximum theoretical absorption of chl *a* in solution (i.e. unpackaged) at 675 nm. When enclosed within a modelled cell, this results in a biophysically consistent relationship between the c_i and cell volume (dictated by cell size) - observable as the "package effect" (Bricaud *et al*., 1995). Secondly, the particle refractive indices are not independent of each other. They are mathematically related as described by the Kramers Kronig relations (Toll, 1956), resulting in particulate absorption and scattering characteristics that are biophysically consistent as they are in nature.

In this study, the UCT-CSIR EAP model will be used in a forward direction, varying the biophysical input parameters (focusing on [chl *a*], D_{eff} and c_i, as constrained by measurements and published parameterisations of these quantities) to investigate their effect on the resulting optical properties and inform on the interpretation of corresponding bulk optical measurements, both *in situ* and satellite-derived.

2.1.2. Considerations for use of the EAP in the Southern Ocean

The primary model input from which all IOPs are derived is the imaginary refractive index of a single cell. Closely related to a particle's absorption characteristics, this input must adequately represent the dominant light harvesting pigments of the assemblage as a whole. For the most part, phytoplankton absorb strongly at 440 nm and 675 nm as characteristic of the ubiquitous primary light harvesting pigment chl *a*. It should be noted that for this study, a generalised set of fucoxanthin- and peridinin- dominated refractive indices are used to represent accessory pigments in the model. These accessory pigments display similarly broad absorption peaks around 500 nm and are prevalent in diatom and dinoflagellate communities in the SO (Robinson *et al*., 2021). It is however acknowledged that these pigments alone do not represent the likely presence of many other phytoplankton types found in *in situ* measurements. The presence of additional accessory pigments may be discernible as detailed adjustments in the shape of the spectra at high spectral resolution. However, it should be noted that while spectral details of additional pigments may well be observable in the measurements, it is the overall magnitude of the spectra that is of interest in this study in response to the observations of 'depressed' spectra that are specific to the SO (Robinson *et al*., 2021).

The EAP model has been validated in coastal waters where the phytoplankton signal overwhelmingly dominates the optical properties, indicating the model's ability to properly simulate phytoplankton IOPs across a range of functional types (Lain *et al*., 2014; Lain *et al*., 2018). In the Benguela coastal waters of South Africa the biomass can be as high as 300 mg m^{-3} (but mostly around 20 or 30 mg m^{-3}) (Lain *et al*., 2014), and the biomass-driven [chl *a*] is by far the primary driver of the phytoplankton optical signal. Particle size, represented by D_{eff}, is by comparison a secondary influence, due to the massive effect of $b_{b\Phi}(\lambda)$ on the R_{rs} at elevated particle concentrations (Lain *et al*., 2014). In the SO however, where phytoplankton biomass is much lower (typically [chl *a*] < 2 mg m^{-3}), biomass-driven signals are much smaller and will likely not overwhelm the phytoplankton-driven optical contribution to the total in-water IOPs in the same way. The respective roles of D_{eff}, accessory pigments and pigment density - especially that of c_i - have not yet been investigated using the EAP model in the context of the SO. This study represents a new application of the model in a low biomass environment where phytoplankton photophysiology is known to play a significant role in driving their optical properties

(Behrenfeld *et al*., 2008; Graff *et al*., 2016). One aspect of photophysiology well understood to impact on cellular optics is the variability in c_i as a response to growth limitations and in particular to a light limiting environment (Behrenfeld *et al*., 2008).

In the EAP model, basic adaptation in phytoplankton photophysiology (or photoacclimation) is represented by variability in the c_i, with an increase in c_i observed to accompany photoacclimation in response to low light conditions (Anning *et al*., 2000; García-Camacho *et al*., 2012; Zonneveld, 1998). It is known that the SO is typically light limited (more so in winter than in summer) due to high latitude (low sun angles), cloudiness and deep mixed layers (Lovenduski *et al*., 2005). In the comparatively low biomass of the SO, we can thus expect that the phytoplankton optics will be more sensitive to changes in physiology and that the c_i will likely be higher in winter than in summer.

The first objective of this study is to parameterise the model appropriately for these different environmental conditions (see Objective 1). This is done by using *in situ* measurements of [chl *a*] and assemblage D_{eff}, to constrain the EAP model inputs so that it may generate a range of IOPs for plausible assemblages in the SO (as evidenced by measured IOPs). There do not exist, however, measurements for the critical parameter of c_i, and the appropriate range of values for this quantity must be inferred from the comparison of model output with $a^*_{\Phi}(\lambda)$ measurements.

Due to different seasonal phytoplankton assemblages (as evidenced by the differences in measured D_{eff} - accessory pigment variability is neglected here) as well as known variability in seasonal light environments, the model is parameterised separately for summer and winter.

Measured [chl *a*] concentrations and Coulter counter PSDs (despite only representing particulates between 2 and 60 μm in diameter) provide the primary constraining inputs into the phytoplankton IOP model. The remaining input parameter, c_i, is unknown. Of all the *in situ* data, it is only the [chl *a*] and the $a_{\Phi}(\lambda)$ (i.e. the subtraction of depigmented $a_p(\lambda)$ from the total), that can be understood to represent the phytoplankton assemblage alone. As the sole available phytoplankton-specific IOP, the filter pad derived $a_{\Phi}(\lambda)$ will be used as the target for model simulation in the process of determining the unknown biophysical parameter of c_i .

Phytoplankton cell size is well understood to impact upon the magnitude of their absorption spectra, with flattened shapes observed for larger cell sizes (Ciotti *et al*., 2002). In the following investigations, it is assumed that the particles described by the Coulter counter between 2 and 60 μm are characterising all phytoplankton (i.e. that there is an insignificant contribution of phytoplankton from < 2 μm and > 60 μm). Where the

depression of measured $a^*_{\Phi}(\lambda)$ can no longer be explained without increasing D_{eff} beyond that is measured, we understand that the remaining parameter to be adjusted is that of the c_i.

The assumption that all particles captured in the 2-60 μm size range are phytoplankton, and building a modelled assemblage accordingly, maximises the modelled phytoplankton contribution to the bulk seawater IOPs (ignoring any contribution from the non-algal component). While acknowledged as an unsatisfactory assumption to make, the effect is to overestimate the phytoplankton contribution to the particle assemblage rather than underestimate it. In the context of the bulk IOPs this allows us to describe the maximum possible phytoplankton optical signal and assert an upper limit for the phytoplankton contribution to the IOPs.

There is undoubtedly some detritus present, but the shape of the size distribution barely changes with the subtraction of a theoretical detrital component, which is assumed to follow a -4 exponential slope. When this detrital correction is made, the volume of particles in the distribution drops, but the effective diameter (and the model input in this study) is hardly impacted. Thus it can be assumed that the Coulter counter captures a fair representation of the shape of the phytoplankton size distribution. The Coulter counter data shows that in summer there are no particles counted larger than 35 μm in the SO, and in winter there are no particles larger than 10 μm. While there is no data to determine the lower limit of phytoplankton sizes (smaller than 2 μm), the complete lack of any particles over the stated maxima supports the idea that most of the phytoplankton fall under the upper limit of the Coulter counter range.

In nature, the quantity of chl *a* in each cell adjusts in response to changing environmental conditions as a physiological response to maximise photosynthesis. Light limitation in particular drives an increase in cellular pigment concentration (Anning *et al*., 2000). Light is known to be the primary driver of c_i changes, nutrients generally to second order (Behrenfeld *et al*., 2003, Graff *et al*., 2016). It is not well quantified in the literature by how much c_i varies within any given assemblage. Literature values of c_i under favourable growth conditions have however been reported to range between 0.1 and 6 kg m^{-3} (Agusti 1991), depending largely on species and cell volume, but also, importantly, on irradiance (Finkel *et al*., 2004). Broadly speaking, the summer phytoplankton assemblages can be expected to be less light limited than in winter, thus a lower c_i would be expected in summer. The additional influences of nutrient (especially iron) limitation are acknowledged, but are beyond the scope of this study.

2.2. *In situ* Measurements

2.2.1. Data Collection

Data were collected during the course of 3 cruises in the SO aboard the SA Agulhas II research ship as part of the Southern Ocean Seasonal Cycle Experiment (SCALE). The winter cruise ran from 25 July 2019 - 3 August 2019, and the two Summer cruises (Leg 1 and Leg 2) took place from 11 December 2019 to 14 January 2020 (Leg 1), and 25 January 2020 to 17 February 2020 (Leg 2) (Figs. 1(a), (b) and (c)). The *in situ* measurements collected during these cruises included [chl *a*], particle size distributions and particulate absorption. The particle sizing and particulate absorption measurements are bulk measurements, that is, comprising both algal and non-algal particulate, whereas [chl *a*] reflects a measurement of phytoplankton alone.

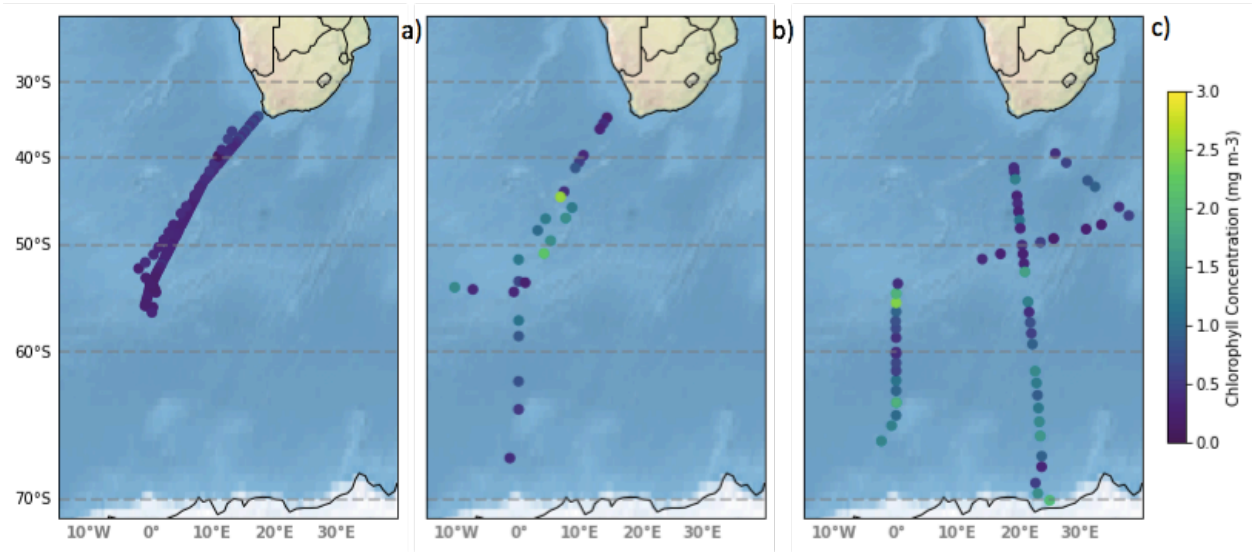

Figure 1: Depicts the stations sampled on the SCALE a) Winter, b) Summer Leg 1 and c) Summer Leg 2 cruises. The colour of the dots reflect ambient [chl a*].*

2.2.2. Chlorophyll *a*

A fluorometric method was used to measure [chl *a*] as per Welschmeyer *et al*., (1994). 500 ml surface water samples were collected from the ship's scientific sea water supply and filtered through a Whatmann 0.7 µm 25mm glass fibre (GF/F) filter. Filters were placed in a glass vial containing 8 ml 90 % acetone and stored at -20°C for about 12-24 h in the dark. Samples had to acclimate to room temperature before the raw chl *a* fluorescence was measured. Fluorescence was measured using a Turner Trilogy Benchtop Fluorometer (non-

acidification module). By using a standard chl *a* dilution calibration, the chlorophyll fluorescence was converted to [chl *a*] (Moutier *et al*., 2019).

2.2.3. Particulate Absorption

Samples of 2000 ml seawater were filtered through 25 mm GF/Fs (0.7 µm nominal pore size). Filters were placed in petri dishes, flash frozen in liquid nitrogen, wrapped in tin foil and stored at -80°C for analysis on land. Post-cruise, the samples were defrosted and the total particulate absorption $a_p(\lambda)$ was measured using a Shimadzu UV-2501 PC spectrophotometer with an ISR-2200 integrating sphere. The design of the spectrophotometer allows the transmitted and most of the scattered light to be collected and measured (Kishino *et al*., 1985). Spectra were collected at 0.5 nm resolution between 380 and 800 nm. Pathlength amplification correction factors were used as per Stramski *et al*., (2015), following the IOCCG best practice protocols (IOCCG Protocol Series, 2018).

In order to obtain the absorption by depigmented particulates, the filters were submerged in 90 % methanol for 24 h (Wang *et al*., 2015). The absorption of depigmented (non-algal) particles, $a_{NAP}(\lambda)$, was then measured by repeating the transmission-reflection method. $a_{\Phi}(\lambda)$ could then be obtained by subtracting $a_{NAP}(\lambda)$, from $a_p(\lambda)$ (Cleveland and Weidemann, 1993).

A quality control check was applied to the $a_{\Phi}(\lambda)$ data, using the ratio $a_{\Phi}(440)$:$a_{\Phi}(657)$, with data falling outside of the range 1 – 4 being excluded (Sosik and Mitchell, 1995; Roesler *et al*., 1989; Bricaud and Stramski, 1990; Neukermans *et al*., 2016). Negative data were also rejected. $a^*_{\Phi}(\lambda)$ (m^2 mg) was derived by dividing $a_{\Phi}(\lambda)$ by the corresponding measured [chl *a*] in mg m^{-3}.

Deriving $a_{\Phi}(\lambda)$ via the process of depigmented $a_{NAP}(\lambda)$ is the only straightforward way of characterising a phytoplankton-specific optical property from *in situ* measurements, and so it is this quantity that is used to parameterise the EAP model.

2.2.4. Particle Size Distributions (PSDs)

Particle size analysis was performed using a Beckman Coulter-Multisizer with a 140 µm aperture tube counting particles between 2-60 µm enumerated within 400 size bins. 40 ml of seawater was analysed at each station (20 runs of 2 ml per run). Blank measurements were made in the same way using 0.2 µm isopore polycarbonate filtered seawater generated from the corresponding sample. The mean blank from each station was subtracted from each sample mean. Particle counts were used to calculate the volume of

particles in each size bin (assuming sphericity). By integrating the particle volumes across the size bins, the total particle volume in each sample ($\mu m^3\ m^{-3}$) was obtained. The effective diameter (D_{eff}) is calculated by dividing the total particle volume by the total surface area of particles in the distribution.

2.3 Satellite Data

The OC-CCI ocean colour dataset (Sathyendranath *et al*., 2019) is the most recent community effort to provide a continuous time series of ocean colour data and derived biogeochemical quantities. The OC-CCI data product suite provides a time series of merged satellite data products from 1997 onwards, utilising data archives from ESA's MERIS and Copernicus's OLCI sensors together with NASA's SeaWiFS, MODIS Aqua and NOAA's VIIRS sensors.

The data used in this study were accessed from the ocean colour website[3]. The relevant latitude, longitude and date (bounding box) were entered into the website to encompass the regional and temporal extent of the SCALE winter and summer cruises. The variables of interest that were extracted were as follows: phytoplankton absorption ($a_{\Phi}(\lambda)$), total particulate backscattering ($b_{bp}(\lambda)$) and chl *a* concentration [chl *a*].

A Python script was used to extract the satellite matchups (M. Smith, *pers comm*) with *in situ* station measurements. The script reads in the station information (date, latitude and longitude) from a spreadsheet and selects a 5 x 5 megapixel box from the satellite netcdf file, centred over the closest latitude and longitude to the given station location, on the relevant date. The megapixel box is used to generate a mean and standard deviation of each *in situ* station's corresponding satellite data product, with the number of valid pixels being reported.

The OC-CCI [chl a] data product is generated for each pixel and weighted according to membership of 14 different water classes as described by Jackson et al., 2017. Class membership of pixels in the SO is dominated by classes 1,10,11,7 and 8 for summer, and 1,10, 7, and 8 for winter. See supplementary Figs. S4 and S5 for the membership water class detail.

The optimal algorithm for water classes 1–7(clearer ocean waters) is OCI, for classes 13–14 (more turbid, highly scattering coastal waters) it was OC3, and for classes 8–12 (generally transitional regions between open ocean and near coastal regions), OC5 was the optimal algorithm used. Therefore, in this study, the dominant algorithms were OCI and OC5.

The Level 3 OC-CCI bio-optical data products are computed using Level 2 Remote Sensing Reflectance (R_{rs}) using the "quasi-analytical" algorithm (QAA) (Lee *et al*., 2002, Lee *et al*., 2009). The QAA performs the inversion of the R_{rs} spectrum to derive the bulk IOPs at 443 nm first, yielding the statistically likely coefficients of backscattering by particles, $b_{bp}(443)$, and total absorption as the combination of phytoplankton absorption, $a_{\phi}(443)$ and absorption from coloured detrital matter, $a_{gd}(443)$, as determined from a large database of

[3] https://www.oceancolour.org/thredds/ncss/grid/CCI_ALL-v5.0-DAILY/dataset.html

in-water radiative transfer simulations. Since the selection of coefficients available depends on those chosen for inclusion in the simulations, this approach may not be appropriate for application in unusual or extreme environments (Lee *et al*., 2002). While the QAA avoids the use of spectral models for $a_{\phi}(\lambda)$ and $a_{gd}()$ coefficients, the radiative transfer simulations that the partitioning is based on, for total absorption into $a_{\phi}(\lambda)$ and $a_{gd}()$ portions assumes some covariance between these quantities (Lee *et al*., 2002). This is a common assumption which is widely employed, with no evidence to suggest inapplicability to the SO.

Chapter 3

3. Results and Observations

3.1 Addressing Aim 1: Identifying the Drivers of the Observed Flattened Absorption Spectra in the Southern Ocean

The primary aim here is to clarify what is the dominant driver of the observed flattened $a^*_{\Phi}(\lambda)$ characteristic of SO phytoplankton as reported by Robinson *et al*., (2021), in terms of pigment density and/or cell size.

In the EAP model, light stress-induced physiological changes can be represented by adjusting the c_i, which will be shown to subsequently alter the amplitude of the absorption spectra. A systematic approach to varying this quantity in the model was used, with a c_i of 5 kg m^{-3} resulting in the best fit modelled $a_{\Phi}(\lambda)$ when compared to measured $a_{\Phi}(\lambda)$ for summer (see Fig. 2(a) and (b)). Laboratory observations of mid-sized species under high light conditions (Stramski *et al*., 1993) and known photoacclimation effects (Behrenfeld *et al*., 2008) support a reasonable value of 5 kg m^{-3}.

The best fit was determined by eye / visually, by comparing the spectra of the model and the spectra of the measurements. The c_i was systematically varied until the spectra of the model matched the spectra of the measurements. It is acknowledged that this is not an optimally rigorous approach, but the most variability in IOPs occur when the c_i is small, and so a best fit by eye is quite straightforward when varying c_i as an integer value. When the c_i gets higher, there is a point at which the variability in IOPs becomes marginal and increasing the c_i further has no further discernible impact on the IOPs. Thus, determining the best fit is possible by eye, as this inflection point is seen.

It should be acknowledged that methodological differences in sample analysis, such as the choice of pathlength amplification factors for $a_p(\lambda)$ measurements (Mitchell *et al*., 1991; Clementson *et al*., 2001), can also contribute to apparent dissimilarity in $a^*_{\Phi}(\lambda)$ from high latitude SO compared with that from other oceans, although these effects would likely be much smaller than the differences observed.

It should also be noted that this study is not an attempt to validate the model in SO waters. The objective is rather towards gaining a mechanistic understanding of the relative impacts of light limitation and phytoplankton photophysiological changes on the IOPs, given the known difference in growth conditions between winter and summer.

3.1.1. Summer

The summer *in situ* measured $a_{\Phi}(\lambda)$ and $a^*_{\Phi}(\lambda)$ (i.e. $a_{\Phi}(\lambda)$ per unit chl *a*) are depicted in Figs. 2(a) and (e). The EAP modelled data represent the $a_{\Phi}(\lambda)$ spectrum of each station simulated with measured Coulter counter D_{eff} and measured [chl *a*] as inputs, and a best-fit c_i of 5 kg m^{-3} as described previously. Eight of the absorption spectra displayed negative measurements that were subsequently removed from the dataset (see Supplementary Fig. S1). One very high biomass station (10.387 mg m^{-3}) at South Georgia displayed an anomalous $a_{\Phi}(\lambda)$ spectrum and was also excluded with the rationale of it being an outlier with respect to the chl range of the rest of the dataset (between 0.199 and 2.572 mg m^{-3}). Three of the spectra had elevated signals at 400 nm (see Supplementary Fig. S1), which suggests incomplete pigment extraction from the total particulate filter pad. Absorption in the blue with this approximately exponential shape is usually an indicator of $a_{NAP}(\lambda)$. These three spectra were also subsequently removed from further analyses.

Ignoring these twelve spectra (negative, anomalous or with incomplete pigment extraction, see Supplementary Fig. S1), the corresponding modelled data, Fig. 2(d), compare favourably to the measured in terms of range, Fig. 2(c), bearing in mind that the measurements represent samples from a substantial range of latitudes. The cluster of spectra representing the majority of the summer measurements is concentrated under a 440 nm peak of approximately 0.04 m^{-1}, which compares well with the majority of the modelled data. The modelled data do of course appear more systematic as small differences in [chl *a*] elicit a more even spread of spectra.

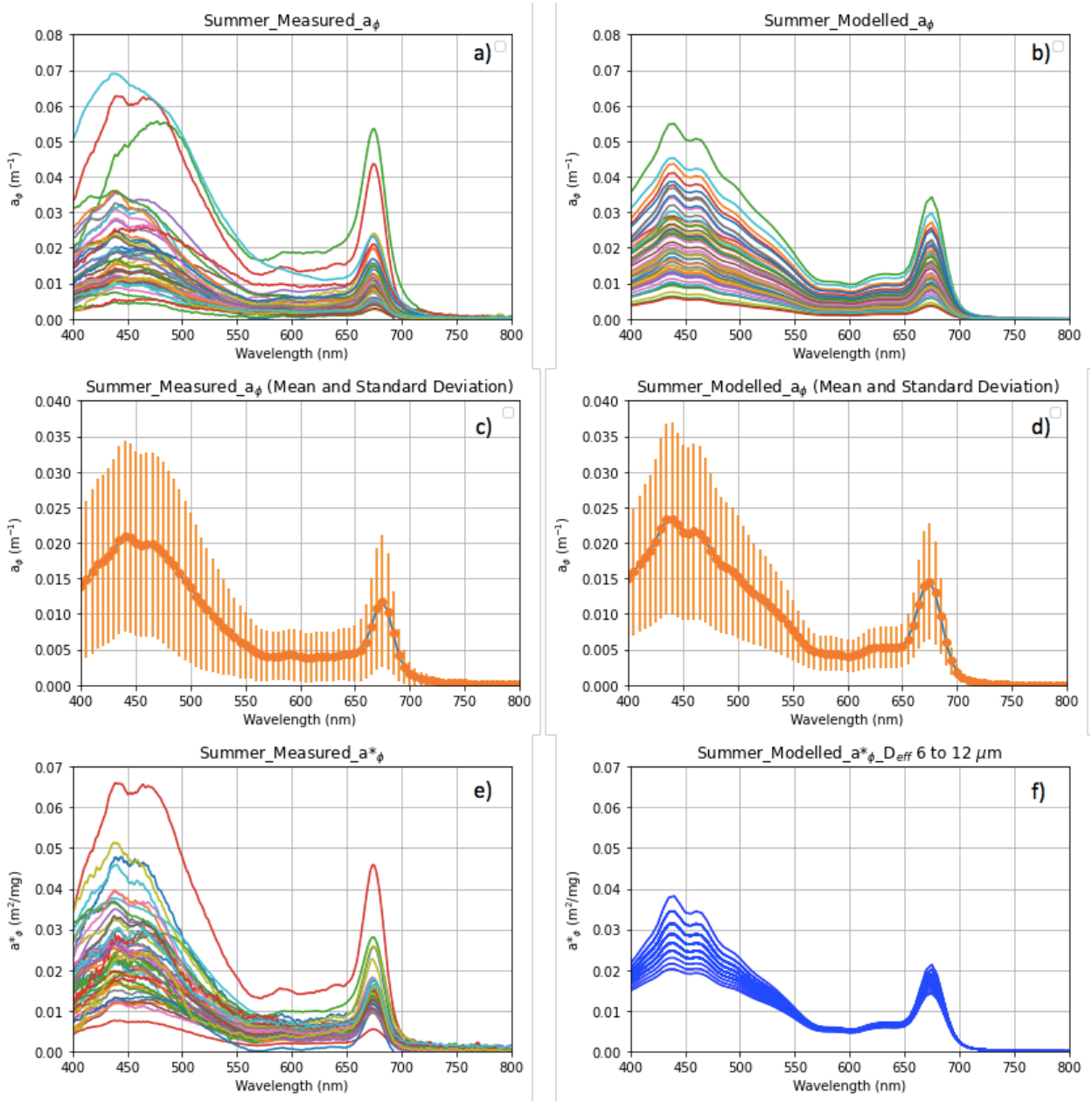

Figure 2: Summer measurements for a) in situ $a_\Phi(\lambda)$ compared to b) EAP model $a_\Phi(\lambda)$ spectra. c) depicts the mean and standard deviation of the measured $a_\Phi(\lambda)$, while d) depicts the mean and standard deviation of the modelled $a_\Phi(\lambda)$ for the same stations. e) presents measured $a^*_\Phi(\lambda)$ compared to f) EAP modelled $a^*_\Phi(\lambda)$ for the same stations. All EAP modelled spectra for summer are generated with a c_i of 5 kg m^{-3}.

The metric of $a^*_\Phi(\lambda)$ removes the effect of biomass from the magnitude of the absorption spectra, although as will be shown, dividing by [chl *a*] is not the same as accounting for cell abundance. Measured $a^*_\Phi(\lambda)$ reveals naturally occurring cell size variability as well as pigment variability, in type and in concentration. Modelled $a^*_\Phi(\lambda)$, on the other hand, reveals only the variability in absorption due to D_{eff} while the c_i is assigned a static value in

the model. It is therefore to be expected that the range of variability in the measured data should be significantly wider than the modelled, and this is evidenced in Fig. 2(e) and 2(f).

The modelled $a^*_{\Phi}(\lambda)$, as presented in Fig. 2(f) is more constrained with respect to the *in situ* $a^*_{\Phi}(\lambda)$ (Fig. 2(e)), likely due to precision in the modelled D_{eff} parameter versus naturally occurring variability in community size structure and also in pigment composition, which is not explicitly addressed here (Lohrenz *et al.,* 2003). The *in situ* $a^*_{\Phi}(\lambda)$, Fig. 2(e), notably displays a larger range of absorption and is in particular a bit higher near the chl *a* absorption maximum at 675 nm, possibly indicating a range of variability in c_i not accounted for in the model, but which would be expected in nature.

Despite these observations, there is fair correspondence between the cluster of measurements representing the majority of stations, and the constrained modelled equivalents. It should be noted that for the modelling, a minimum and maximum effective diameter of 6 and 12 μm are used respectively, chosen to be as close to the minimum and maximum measured effective diameters as possible. A possible reason for some measured spectra lying well below the minimum modelled absorption (corresponding to a 12 μm D_{eff} assemblage), is that the c_i could in nature be higher than the nominal 5 kg m^{-3} chosen for this investigation. A c_i higher than 5 kg m^{-3} would result in modelled spectra that were even further depressed.

3.1.2. Winter

To illustrate the need for careful parameterisation of the model in acknowledgement of seasonal light limitations on phytoplankton growth and the subsequent changes in phytoplankton physiology and pigment density, winter $a_{\Phi}(\lambda)$ was first modelled using a c_i of 5 kg m^{-3} (as per the summer model parameterisation).

The subsequent winter *in situ* measured $a_{\Phi}(\lambda)$ and modelled $a_{\Phi}(\lambda)$ (using a c_i of 5 kg m^{-3}) are depicted in Figs. 3(a) and (b).

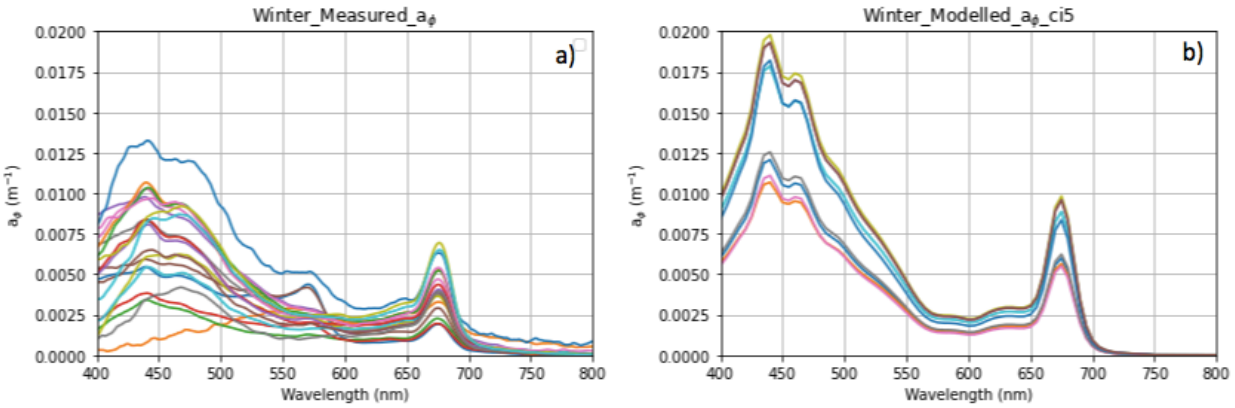

Figure 3: a) Winter measured $a_\Phi(\lambda)$ b) Winter modelled $a_\Phi(\lambda)$ using a c_i of 5 kg m^{-3}.

Note that, as with summer, there were three obvious outliers in the measured data which were removed i.e. as they were negative, anomalous or with incomplete pigment extraction (refer to Supplementary Fig. S2 for the complete set of measurements). The modelled $a_\Phi(\lambda)$ was again simulated using measured [chl *a*] and the Coulter counter derived D_{eff}. When the winter $a_\Phi(\lambda)$ is modelled using the same value for the c_i parameter as summer (5 kg m^{-3}), the EAP model clearly overestimates $a_\Phi(\lambda)$ (Fig. 3(b), maximum is about 0.02 m^{-1}) when compared to *in situ* measured absorption (Fig. 3(a), maximum is about 0.013 m^{-1}). With the understanding that the c_i parameter represents photophysiology-induced variability in photosynthetic pigment density in the model, it is logical that the c_i would need to be increased further for appropriate parameterisation of the EAP model in polar winter conditions.

The systematic approach of incrementally increasing the c_i input parameter was repeated, with a best fit for the resulting simulated $a_\Phi(\lambda)$ accounting for a c_i of 12 kg m^{-3} in winter.

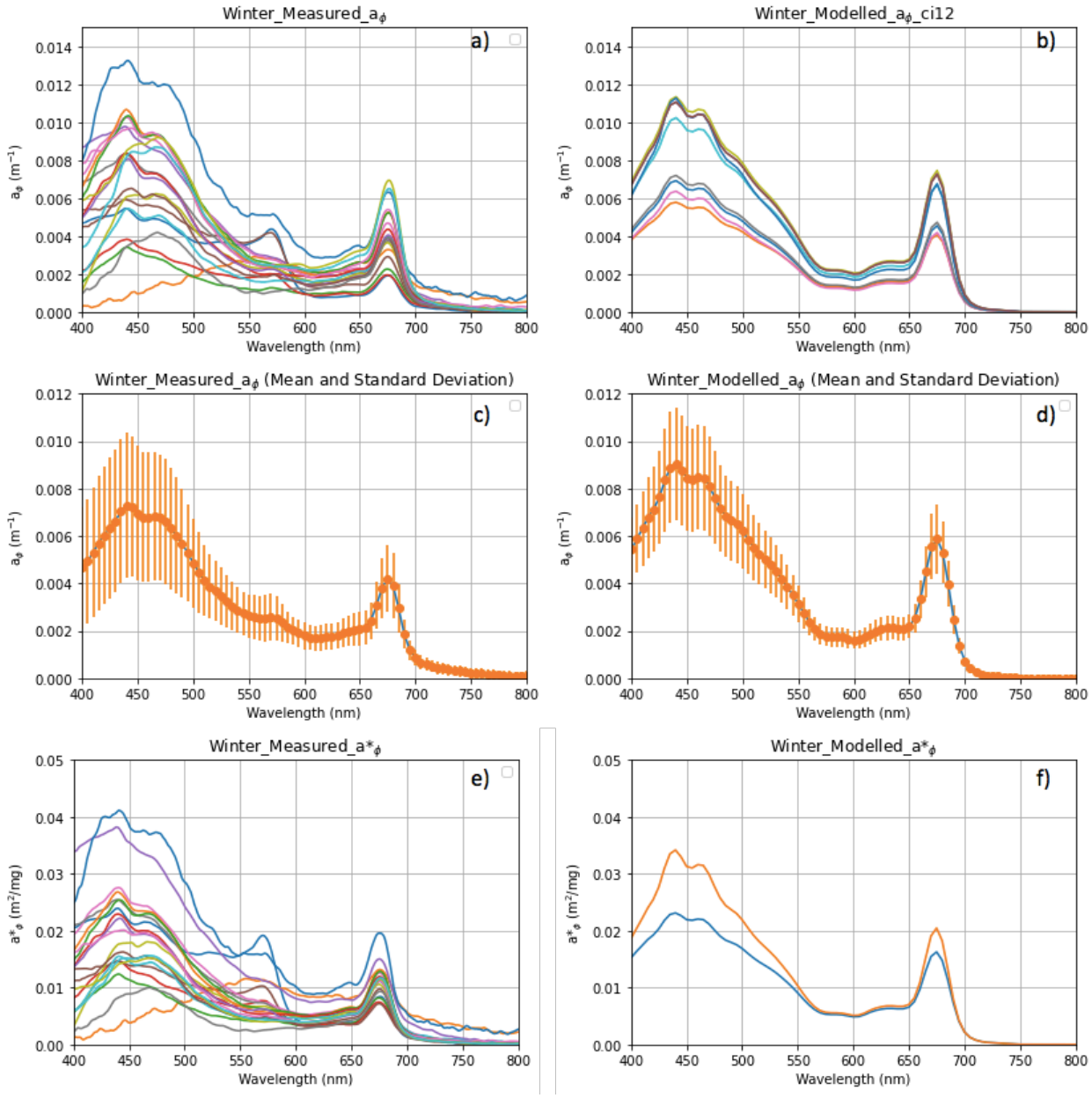

Figure 4: Winter (a) in situ *measured $a_\Phi(\lambda)$ spectra that are compared to (b) EAP model derived $a_\Phi(\lambda)$ spectra (c) mean and the standard deviation of the measured $a_\Phi(\lambda)$ (d) mean and the standard deviation of the modelled $a_\Phi(\lambda)$ (e) measured $a^*_\Phi(\lambda)$, and (f) EAP modelled $a^*_\Phi(\lambda)$ derived for phytoplankton of D_{effs} of 3 and 4 µm. All EAP modelled spectra for winter are generated with a c_i of 12 kg m^{-3}.*

The winter *in situ* measured $a_\Phi(\lambda)$ are presented with their modelled counterparts in Figs. 4(a) and (b), and their respective means and standard deviations in Figs. 4(c) and (d). The corresponding $a^*_\Phi(\lambda)$, measured and modelled, are depicted in Figs. 4(e) and (f) with the modelled spectra reflecting the minimum and maximum measured D_{effs} of 3 and 4 µm.

It can be deduced from Fig. 4 that when the EAP model is adjusted for an anticipated physiological response to low light conditions (by increasing chl *a* pigment packaging with a subsequent increase in c_i to 12 kg m^{-3}), that the EAP model is able to adequately reproduce $a_\Phi(\lambda)$ comparable to that of the measured *in situ* $a_\Phi(\lambda)$, with reduced variability as discussed for the summer data. The *in situ* winter measured $a_\Phi(\lambda)$ in Fig. 4(a) and the corresponding EAP modelled spectra, Fig. 4(b), all fall between 0 and 0.015 m^{-1}. It can also be observed that there is a close match between the range of measured $a^*_\Phi(\lambda)$, Fig. 4(e), and modelled $a^*_\Phi(\lambda)$, Fig. 4(f), with all spectra falling between 0 and 0.05 m^{-1}, and with the majority less than 0.03 m^{-1}.

3.1.3. Understanding the Drivers of Spectral Flattening: Pigment Packaging versus the Package Effect

As stated in Section 2.1.1, the EAP model maintains a biophysically consistent relationship between c_i and cell volume. As cell size (and hence volume) increases, the cross-sectional absorption efficiency decreases as intracellular chl *a* pigment is increasingly shielded from incoming light by additional cellular material - observable in the optics as the flattened $a^*_\Phi(\lambda)$ characteristic of the "package effect" (Bricaud *et al*., 1995). This is the "more packaged" phytoplankton pigment identified in Robinson *et al*., (2021) as being driven by large cell sizes.

Confusingly, the changes in c_i driven by photophysiological responses to the light environment, are typically referred to as "pigment packaging", but this is an entirely different process, which is independent of the size determined "package effect". Rather, "pigment packaging" refers to an increase in pigment density per cell as a photoacclimation response to low light conditions that can also result in depressed $a^*_\Phi(\lambda)$ spectra. As pigment density increases with photoacclimation, the cross-sectional absorption efficiency of each cell increases (Falkowski, P.G., Chen, YB., 2003), as expected, because photoacclimation occurs in order to maximise photosynthesis under low light conditions. However it is worth noting that while each cell absorbs more efficiently (as it is packed with relatively more pigment), fewer cells are needed to comprise a unit of chl *a* as their individual density of this pigment has increased. As such, when measured as a whole assemblage, the total $a_\Phi(\lambda)$ per unit chl *a,* i.e. $a^*_\Phi(\lambda)$ is comparatively less than from a sample with many more cells making up the same [chl *a*].

The EAP model allows for the separation of these two processes and the investigation of their respective impact on the optics of a phytoplankton assemblage. By keeping the c_i constant, the size-driven "package effect" can be observed, while by keeping the D_{eff} constant, the impact of c_i (i.e. photophysiology) driven "pigment packaging" can be

observed. This ability of the model is articulated in Figs. 5(a) and (b), which provides a clear example of how similar spectra can be generated from the two different processes. By using the model to interpret the measured SO data, the interplay and proportional impact of these two drivers of phytoplankton optics (D_{eff} and c_i) can be interrogated.

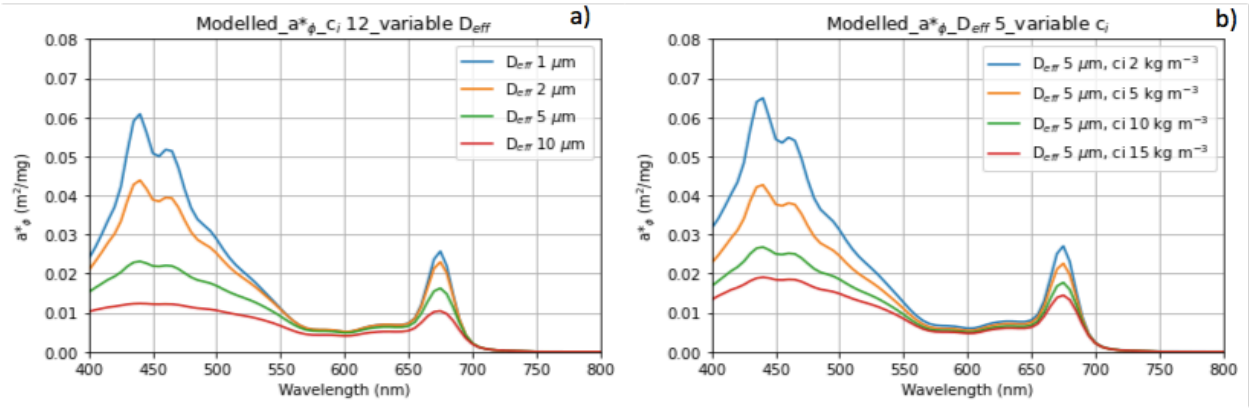

Figure 5: Modelled $a^*_\Phi(\lambda)$ with (a) c_i of 12 kg m^{-3}, and variable D_{eff} and (b) D_{eff} of 5 μm with variable c_i (in kg m^{-3}).

For summer the $a^*_\Phi(\lambda)$ data are modelled in Fig. 6 within the measured D_{eff} range of between 6 (green line) and 12 μm (red line), but without accounting for any photophysiological changes due to light and/or nutrient stress (i.e. with a low c_i of 2 kg m^{-3} as used in the growth favourable conditions of the Benguela region, for example). These are overlaid on the actual *in situ* measurements, also reflecting D_{eff} between 6 and 12 μm, but of course additionally reflecting any photophysiological adaptations found *in situ*.

The growth-favourable $a^*_\Phi(\lambda)$ spectra demonstrate the higher magnitude absorption observed more commonly elsewhere in the world. The blue line shows that to fit with the measured $a^*_\Phi(\lambda)$, an assemblage in favourable growth conditions, would imply a D_{eff} of about 30 μm. This is more than double (2.5 times) the actual measured D_{eff}, which reached a maximum in summer of 12 μm.

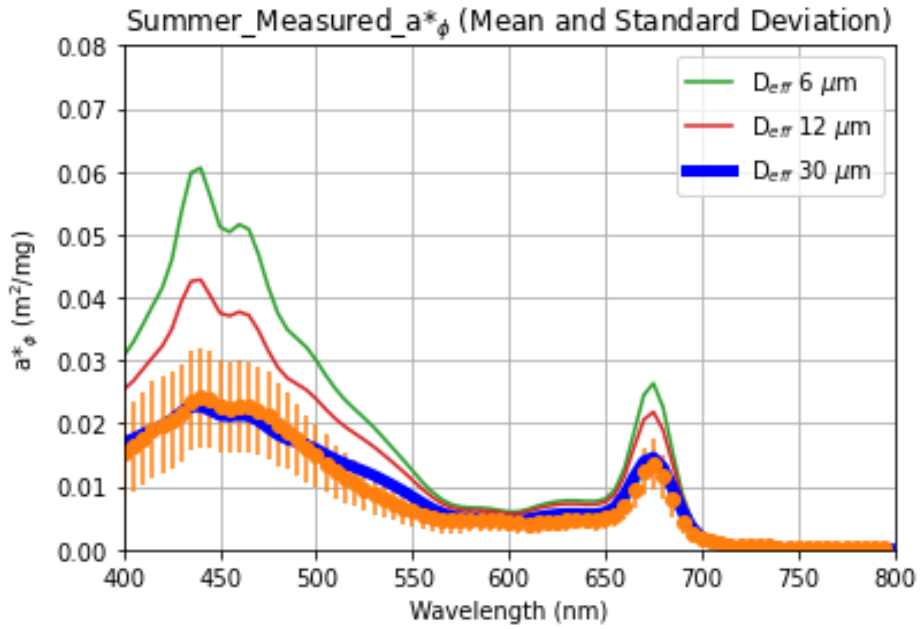

Figure 6: Measured summer $a^*_\Phi(\lambda)$ (mean and standard deviation, in orange) plotted with modelled $a^*_\Phi(\lambda)$ with a c_i of 2 kg m^{-3} representing a favourable growth environment for a D_{eff} of 6 µm (green) and 12 µm (red) (as per the range of measured D_{eff}). Modelled $a^*_\Phi(\lambda)$ with a D_{eff} of 30 µm (blue) is the best fit to the measured data.

Similarly, the winter data are modelled in Fig. 7 within the measured D_{eff} range of between 3 µm (green line) and 4 µm (red line) with a low c_i of 2 kg m^{-3} inferring no pigment packaging. Again, a size distribution of D_{eff} of about 30 µm would be required to generate $a^*_\Phi(\lambda)$ spectra within the same order of magnitude as the measured spectra. This is 7.5 times higher than the maximum measured winter D_{eff} of 4 µm.

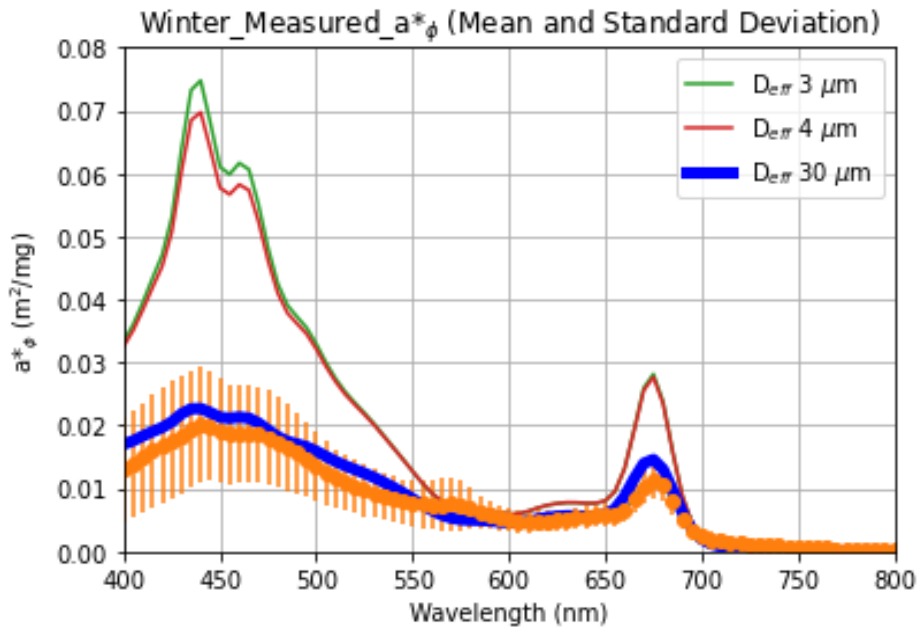

Figure 7: Measured winter $a^*_\Phi(\lambda)$ (mean and standard deviation, in orange) plotted with modelled $a^*_\Phi(\lambda)$ with a c_i of 2 kg m^{-3} representing a favourable growth environment for a D_{eff} of 3 µm (green) and 4 µm (red) (as per the range of measured D_{eff}). Modelled $a^*_\Phi(\lambda)$ with a D_{eff} of 30 µm (blue) is the best fit to the measured data.

It is clear from this analysis that D_{eff} would have to increase to implausibly large cell sizes in order to generate the depressed $a^*_\Phi(\lambda)$ spectra characteristic of both the summer and winter data. This makes it unlikely that the depressed absorption can be attributed to change in cell size (i.e. the package effect). Rather, we can conclude that the primary driver of the depressed $a^*_\Phi(\lambda)$ (similarly observed by Robinson *et al.*, 2021), is more likely a photophysiological response to the characteristically low light conditions of the SO, which drives an increase in cellular pigment (i.e. pigment packaging). There is, however, a large overlap in the characteristics of the measured $a^*_\Phi(\lambda)$ between the seasons despite differences in the measured D_{eff} , with a larger size range being evident in summer. This is because of the opposing effects of D_{eff} and c_i on the $a^*_\Phi(\lambda)$ spectra, which can generate similar spectra from different conditions. For example, in winter, smaller cells elevate the $a^*_\Phi(\lambda)$, while a higher c_i flattens it down. Whereas in summer, larger cells flattens the $a^*_\Phi(\lambda)$, but lower c_i causes an elevation. This sort of ambiguity in $a^*_\Phi(\lambda)$ spectra is discussed further in Section 3.1.4.

3.1.4. Investigating the Satellite OC-CCI $a_\Phi(\lambda)$ Product

Given the characteristically flattened $a_\Phi(\lambda)$ *and* $a^*_\Phi(\lambda)$ spectra observed *in situ* in the SO, the question arises as to whether biogeophysical data product retrieval algorithms applied to

satellite radiometry (more likely parameterised and validated with data from other oceans) are able to capture these distinguishing features.

OC-CCI R_{rs} are provided in five wavebands that extend from 412 to 560 nm (412, 443, 490, 510 and 560 nm). As such, the data does not cover the entire spectrum of *in situ* measurement wavelengths. To begin with, the satellite $a_{\Phi}(\lambda)$ product, Fig. 8(a), is compared with the measured $a_{\Phi}(\lambda)$, Fig. 8(b), for summer. When looking at the range of *in situ* $a_{\Phi}(\lambda)$ measurements over the whole summer cruise alongside the satellite product retrievals over the whole time period, the range of amplitudes observed is comparable. This is clearly observed in the comparison of the means and standard deviation of the *in situ* $a_{\Phi}(\lambda)$ (Fig. 8(c)) and satellite $a_{\Phi}(\lambda)$ (Fig. 8(d)) measurements. However, when only the matchup stations are compared, Figs. 8(e) and (f), it is clear that the satellite tends to overestimate $a_{\Phi}(\lambda)$ relative to what was measured, in particular with regards to station 6 (Fig. 8(e)). Although six satellite and *in situ* matchups were retrieved, only two were viable as the other four *in situ* spectra displayed high absorption in the blue wavelengths which were removed as they displayed the characteristic of incomplete phytoplankton pigment extraction (see Supplementary Figs. S3(a)-(d)). This result, in the context of understanding how sensitive the optics are to photophysiology, suggests that while the OC-CCI product appears to adequately represent the intra-seasonal range of $a_{\Phi}(\lambda)$ over the spatial extent of the summer cruise; on an individual basis, the OC-CCI $a_{\Phi}(\lambda)$ product may not accurately reflect localised photophysiological effects. Although there are only two matchups it appears that the QAA algorithm may have a tendency to overestimate $a_{\Phi}(\lambda)$ in the SO in summer.

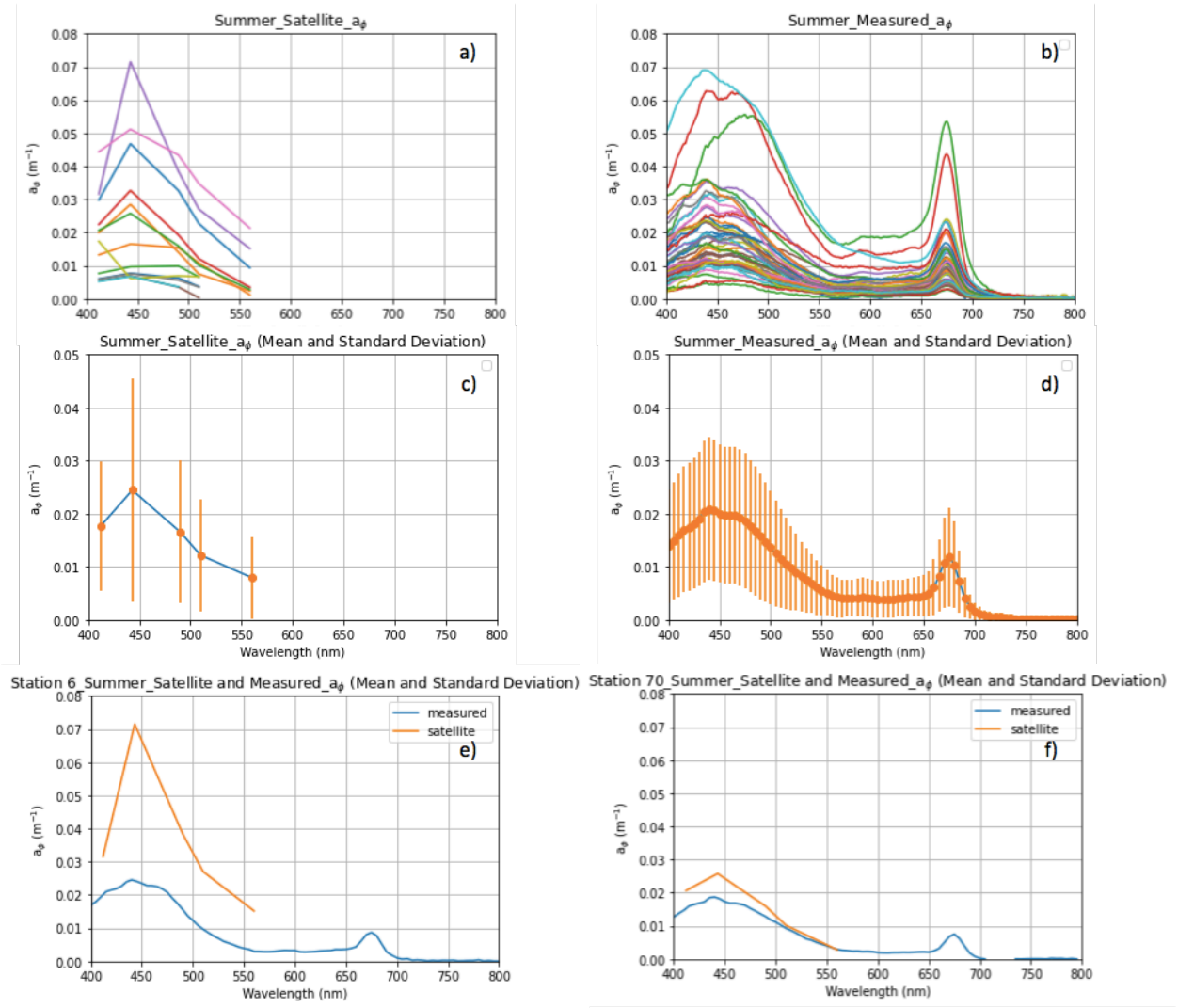

Figure 8: Summer a) OC-CCI satellite derived $a_\Phi(\lambda)$ spectra compared to b) in situ measured $a_\Phi(\lambda)$ spectra. Mean and standard deviation of the c) OC-CCI satellite derived $a_\Phi(\lambda)$ spectra compared to d) in situ measured $a_\Phi(\lambda)$ spectra. The comparisons of satellite derived and measured $a_\Phi(\lambda)$ spectra using only the 2 matchups in time and location are depicted in e) station 6 and f) station 70.

When comparing the [chl *a*] normalised satellite product $a^*_\Phi(\lambda)$ (Fig. 9(a) and (b)) we see that the difference between the satellite and *in situ* product is exaggerated with a larger overestimation of $a^*_\Phi(\lambda)$ relative to what was measured. This is particularly evident from the mean and standard deviation plots which show a 73 % overestimate on average (Fig. 9(c) and (d)).

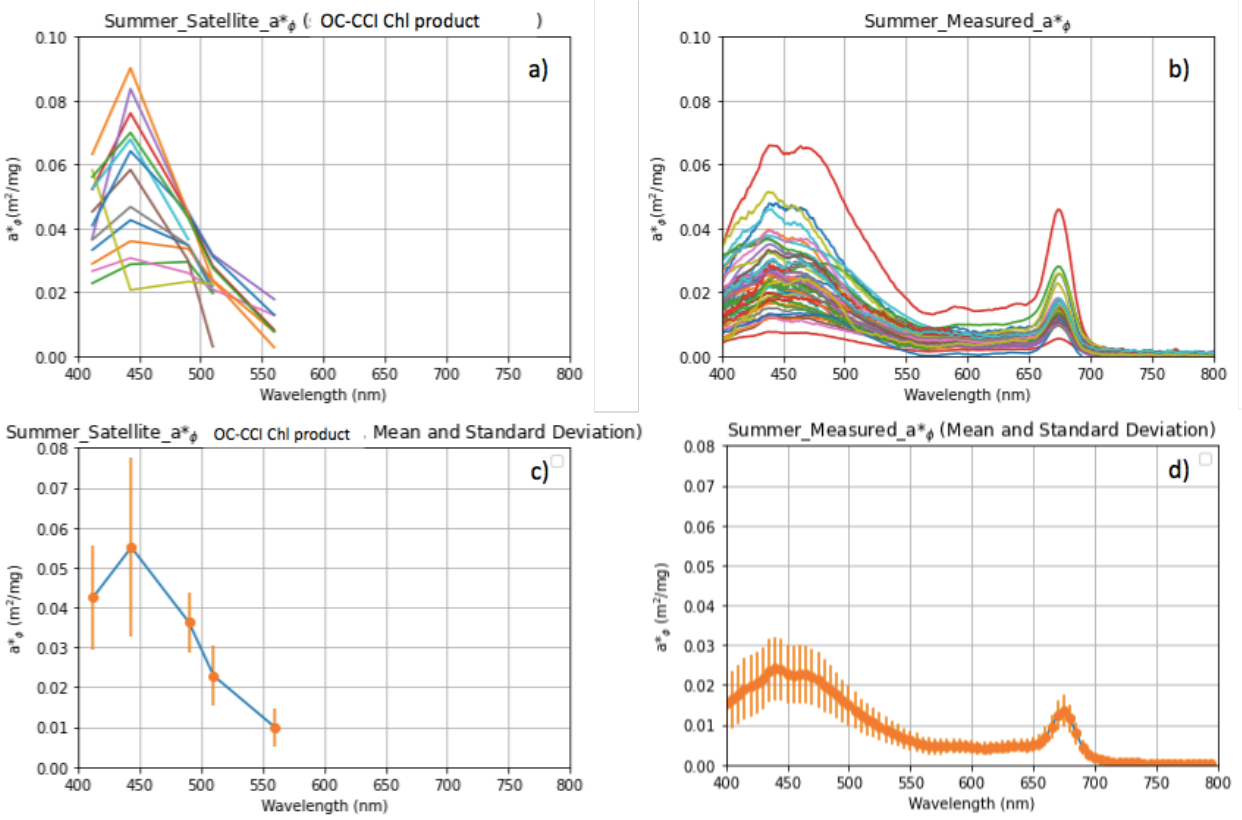

Figure 9: Summer a) satellite a$_{\Phi}$(λ) using satellite OC1 and OC5 algorithm derived [Chl a], b) in situ measured a*$_{\Phi}$(λ), c) mean and standard deviation of a*$_{\Phi}$(λ) using the satellite OC1 and OC5 algorithm derived [Chl a] and d) mean and standard deviation of the in situ measured a*$_{\Phi}$(λ).*

That being said, satellite derived [chl *a*] algorithms have been known to underestimate [chl *a*] when applied to the SO (eg. Johnson et al., 2013; Kahru *et al.*, 2010). This is clearly evident from Fig. 10 which shows a comparison of the 13 *in situ* versus satellite derived [chl *a*] matchups for summer being on average 43 % lower than the *in situ* measured [chl *a*]. However, it is worth noting that this difference was not consistent across all match up stations, with some stations displaying very similar concentrations (e.g. station 1) and others (e.g. stations 2 - 6) where the satellite derived [chl *a*] was indeed slightly higher than *in situ* [chl *a*].

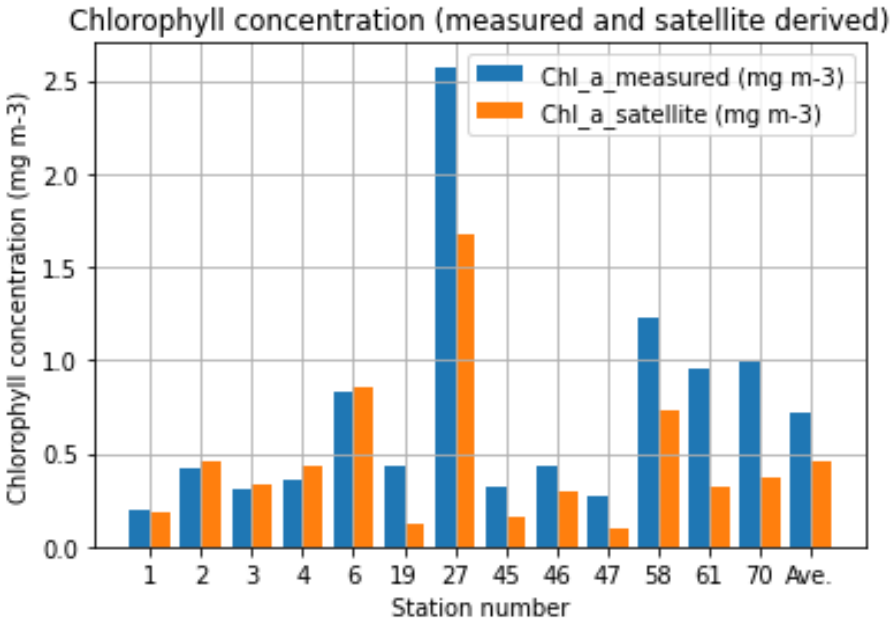

Figure 10: Summer comparison of in situ measured [chl a] versus OC1 and OC5 satellite derived [chl a], with the final bar representing the average of all match up stations.

If we instead use *in situ* measured [chl *a*] to derive $a^*_\Phi(\lambda)$ from satellite (i.e. we normalise the satellite $a^*_\Phi(\lambda)$ product with *in situ* measured [chl *a*] instead of the blended OC-CCI [chl *a*] product), it is clear from (Fig. 11) that the satellite $a^*_\Phi(\lambda)$ spectra become more depressed and closer in range to the measured $a^*_\Phi(\lambda)$. However on average, the satellite $a^*_\Phi(\lambda)$ spectra remain overestimated (40 %) relative to the measured $a^*_\Phi(\lambda)$ spectra.

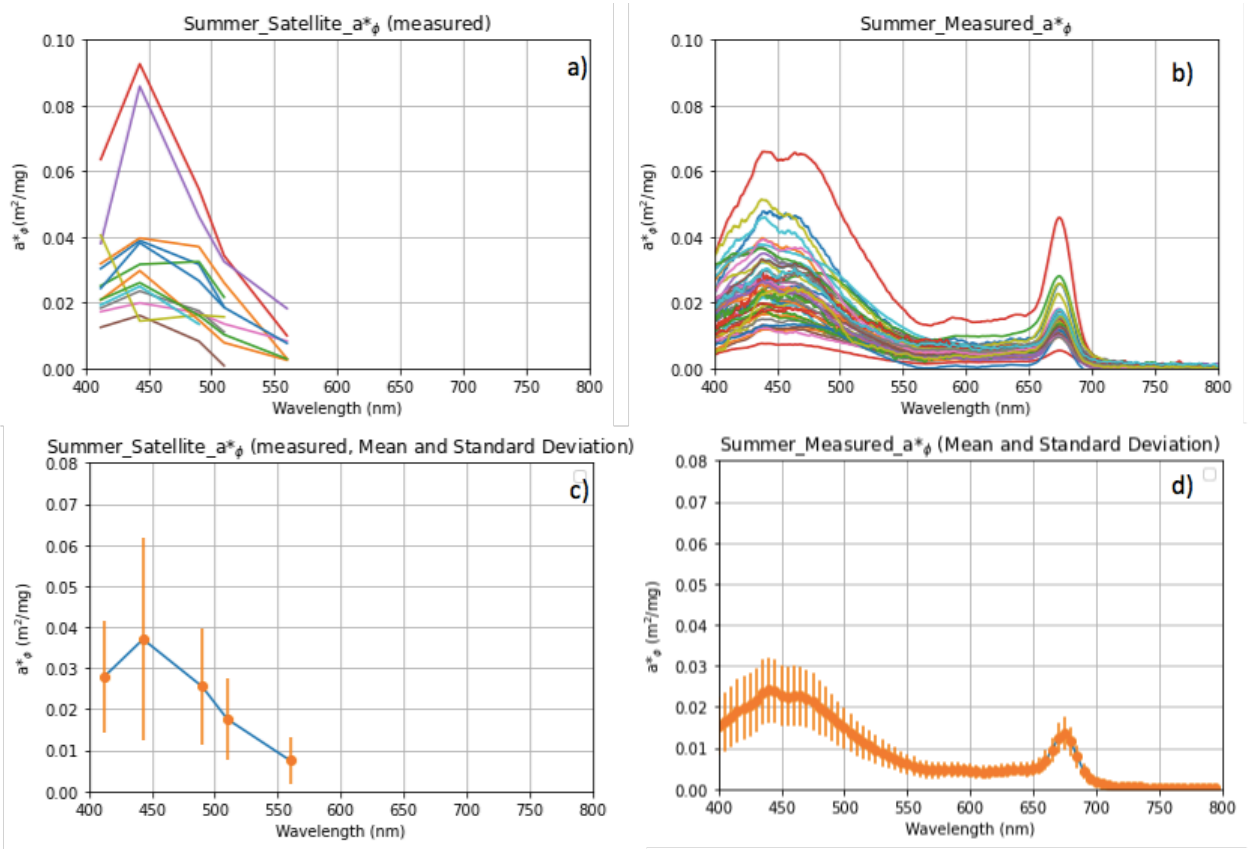

Figure 11: Summer a) satellite $a^*_\Phi(\lambda)$ using measured in situ [Chl a], b) in situ measured $a^*_\Phi(\lambda)$, c) mean and standard deviation of $a^*_\Phi(\lambda)$ using the in situ measured [Chl a] and d) mean and standard deviation of the in situ measured $a^*_\Phi(\lambda)$.

A comparison of the two summer stations where we have matchups in $a_\phi(\lambda)$ (Fig. 12) shows that satellite $a^*_\phi(\lambda)$ calculated from OC-CCI blended [chl *a*] and *in situ* [chl *a*] are very similar for station 6, but much lower for station 70 when calculated from *in situ* [chl *a*] (Fig. 12(a) and (b)). As such, although the approach of using *in situ* [chl *a*] to derive satellite $a^*_\phi(\lambda)$ results in a similar order of magnitude spectra for station 70, this is not the case for station 6 whose $a^*_\phi(\lambda)$ spectra remain substantially overestimated (63 %) by satellite.

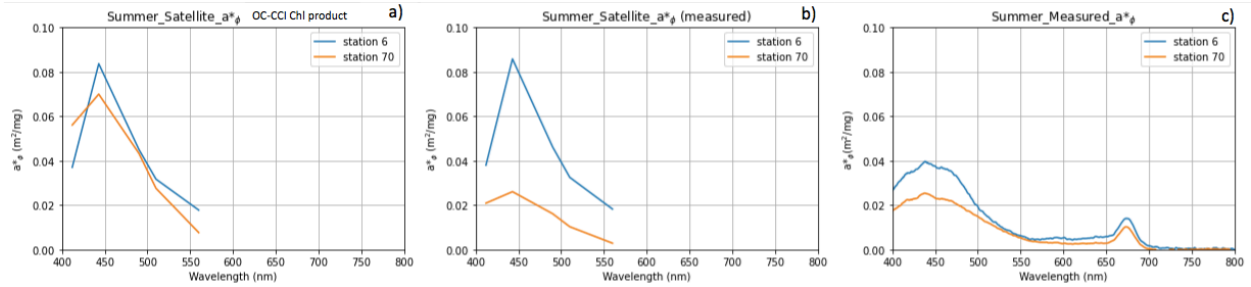

Figure 12: Summer a) satellite derived $a^*_\Phi(\lambda)$ for the matchups stations 6 and 70 using OC1 and OC5 algorithm derived [chl a] and b) using in situ measured $a^*_\Phi(\lambda)$ compared to c) in situ measured $a^*_\Phi(\lambda)$.

A similar comparison was conducted for winter. Unlike in summer, the satellite $a_\Phi(\lambda)$ in winter, Figs. 13(a) and (c), were substantially overestimated (80 % on average) when compared to the measured *in situ* $a_\Phi(\lambda)$, Figs.13(b) and (d).

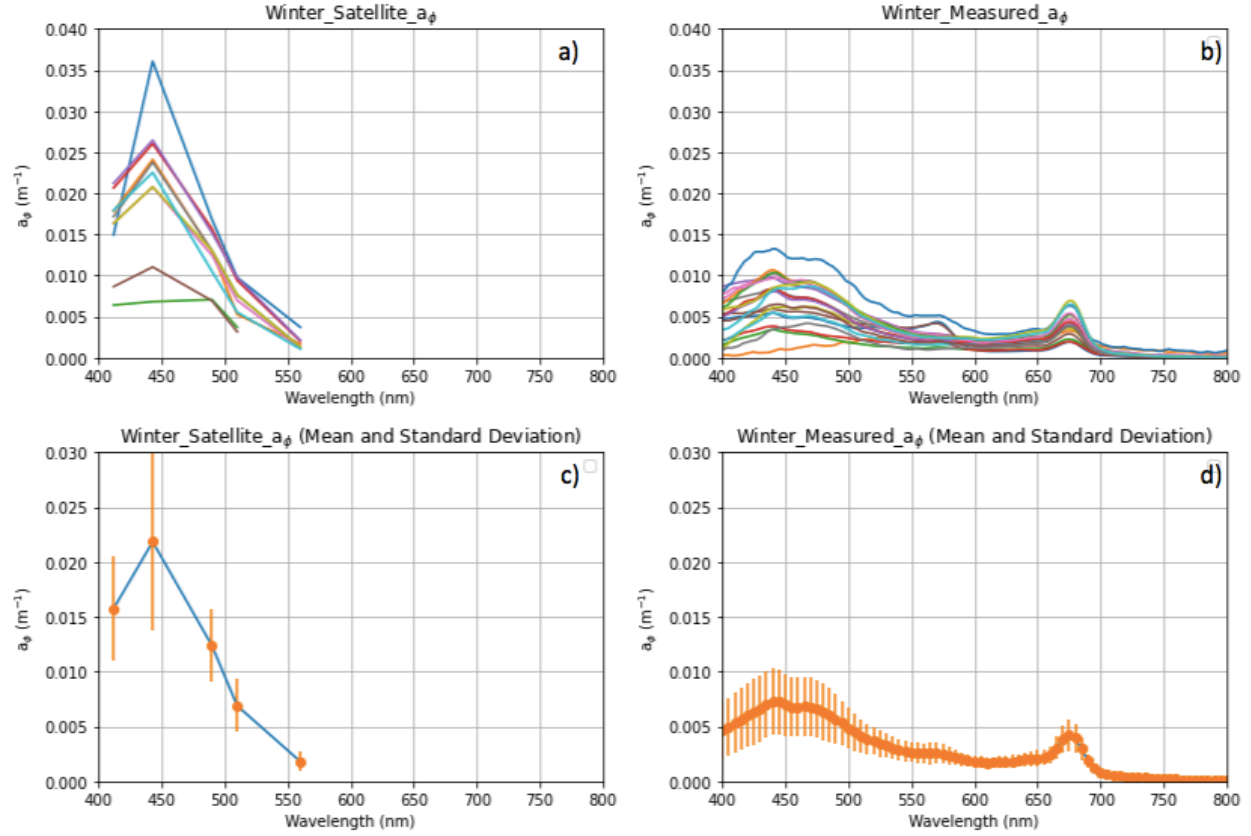

Figure 13: Winter a) OC-CCI satellite derived $a_\Phi(\lambda)$ spectra compared to b) in situ measured $a_\Phi(\lambda)$ spectra. Mean and standard deviation of the c) OC-CCI satellite derived $a_\Phi(\lambda)$ spectra compared to d) in situ measured $a_\Phi(\lambda)$ spectra.

Similarly, when winter satellite derived $a^*_\Phi(\lambda)$ is compared to the winter measured $a^*_\Phi(\lambda)$ (Figs. 14(a) and (b)), the range of distribution is substantially overestimated (which at 98

% difference on average equates to almost double) by the satellite derived product (Figs. 14(c) and (d)).

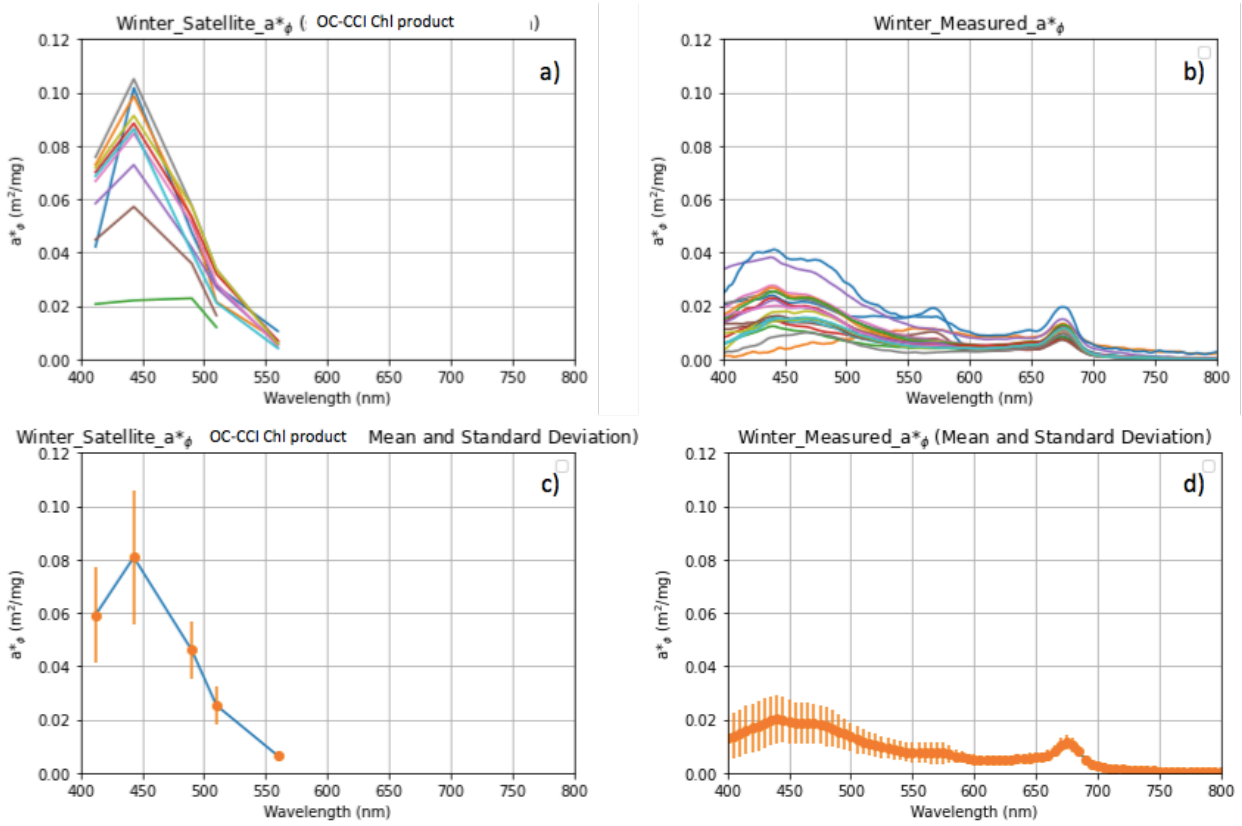

Figure 14: Winter a) satellite $a^*_\Phi(\lambda)$ using satellite OC1 and OC5 algorithm derived [Chl a], b) in situ measured $a^*_\Phi(\lambda)$, c) mean and standard deviation of $a^*_\Phi(\lambda)$ using the satellite OC1 and OC5 algorithm derived [Chl a] and d) mean and standard deviation of the in situ measured $a^*_\Phi(\lambda)$.

In winter, the offset between *in situ* measured [chl a] and satellite derived [chl a] were even more apparent than in summer and consistent across all stations with an average underestimate of [chl a] by satellite of 64 % (Fig. 15).

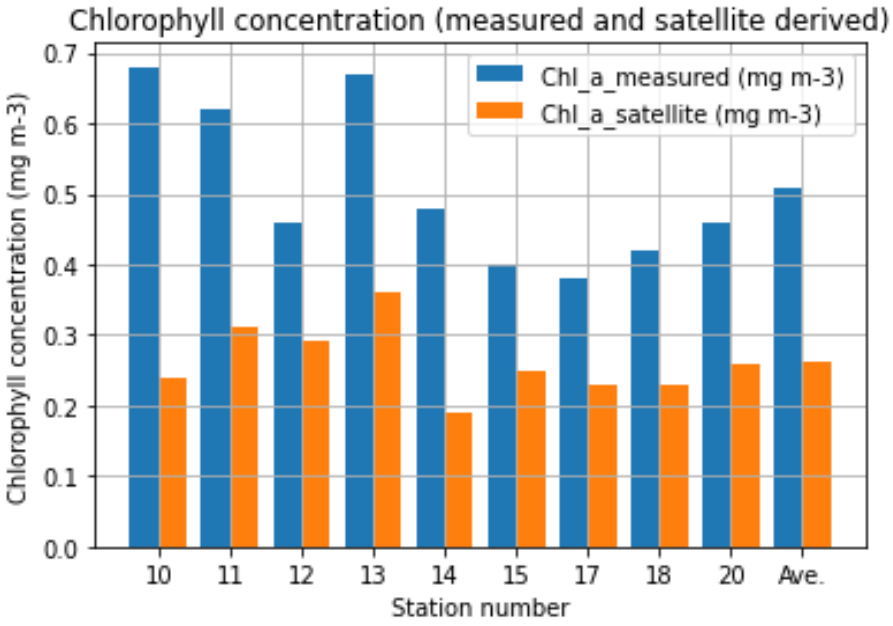

Figure 15: *Winter comparison of in situ measured [chl a] versus OC1 and OC5 satellite derived [chl a], with the final bar representing the average of all match up stations.*

As such, a substantial decrease is observed in the satellite derived $a^*_\phi(\lambda)$ spectra when normalised with *in situ* measured [chl a] (Fig. 16(a) and (b)) as opposed to the blended OC-CCI chl a product . Nonetheless, the overestimation of satellite $a^*_\phi(\lambda)$ remains substantial in winter (44 %) even when *in situ* measured [chl a] is used to normalise $a_\phi(\lambda)$ (Figs. 16(c) and (d)).

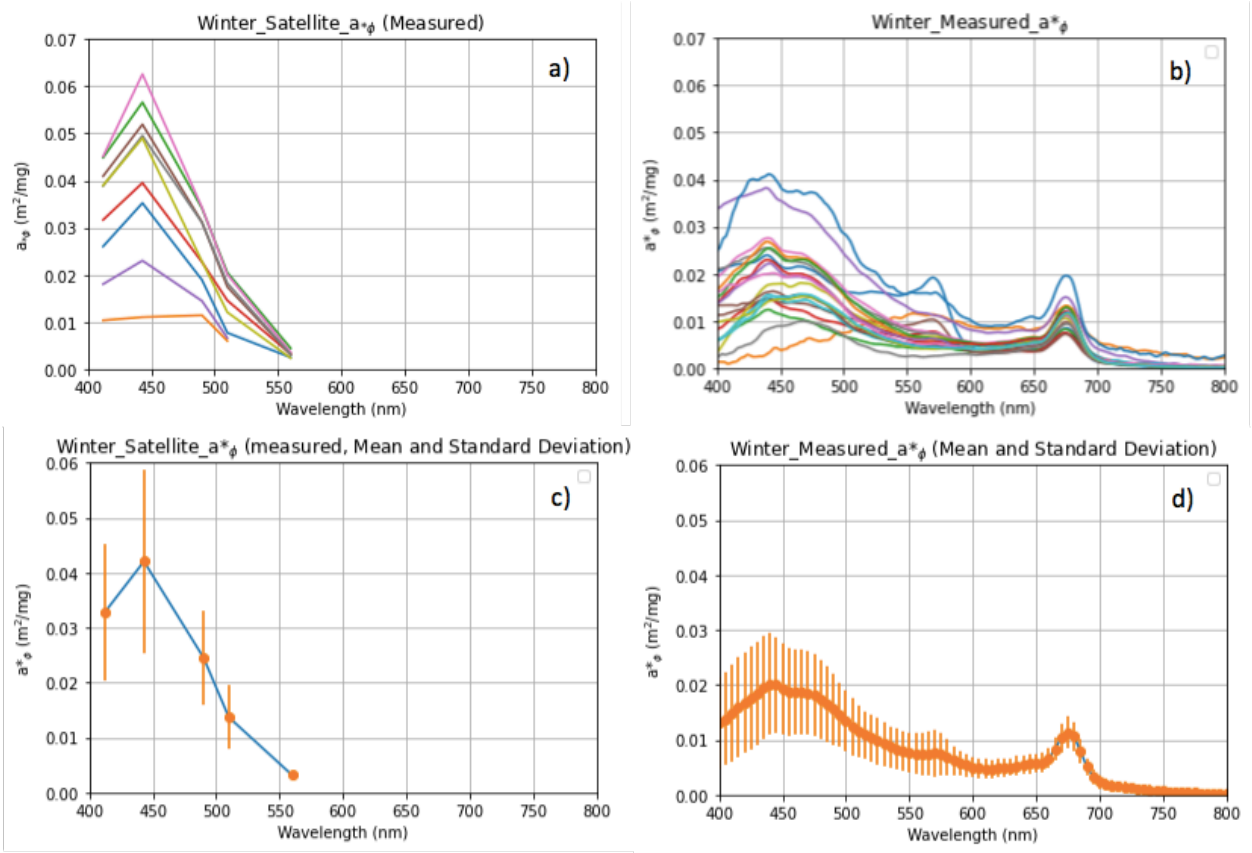

Figure 16: *Winter a) satellite a*$_{\Phi}(\lambda)$ using measured in situ [Chl a], b) in situ measured a*$_{\Phi}(\lambda)$, c) mean and standard deviation of a*$_{\Phi}(\lambda)$ using the in situ measured [Chl a] and d) mean and standard deviation of the in situ measured a*$_{\Phi}(\lambda)$.*

Due to there being no match up stations between satellite and *in situ* $a_{\phi}(\lambda)$ for winter, we instead compare satellite derived $a^*_{\phi}(\lambda)$ from both OC-CCI [chl *a*] and measured *in situ* [chl *a*] with modelled $a^*_{\phi}(\lambda)$ (Fig. 17(c)). This comparison is based on the understanding that the EAP model can approximately represent the winter range of $a_{\phi}(\lambda)$ *with* a c_i of 12 kg m^{-3}, as shown in Fig. 4. Again, the comparison shows that the satellite product tends to overestimate $a^*_{\phi}(\lambda)$ regardless of whether the satellite $a_{\phi}(\lambda)$ product is normalised with OC-CCI [chl *a*] (Fig. 17(a)) or *in situ* measured [chl a] (Fig. 17(b)).

These results imply that the satellite $a_{\Phi}(\lambda)$ product suffers from a similar shortcoming as the model when photoacclimation is not accounted for in low light conditions (i.e. when the model is parameterised with a low c_i) (see Fig. 3(b)).

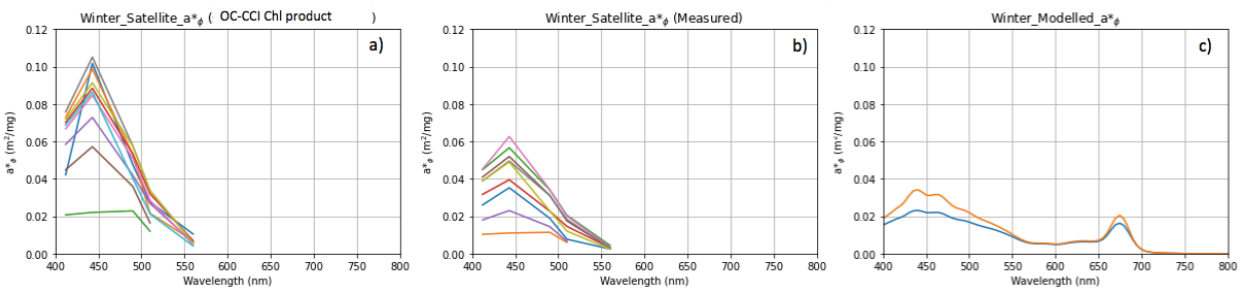

Figure 17: Winter a) OC-CCI satellite derived $a^*_\Phi(\lambda)$ spectra, b) OC-CCI satellite derived $a^*_\Phi(\lambda)$ normalised with in situ measured [chl a] compared to c) modelled $a^*_\Phi(\lambda)$ spectra using a c_i of 12.

This fits with the understanding of the QAA-derived $a^*_\Phi(\lambda)$ being more typical of lower latitudes as a result of the algorithm being parameterised using NOMAD datasets which are under representative of the SO and therefore of the additional optical complexity introduced by divergence of [chl a] and phytoplankton size, and also by variability in c_i due to photoacclimation. Typical low latitude phytoplankton absorption spectra are shown in Fig. 18, from Bricaud *et al.*, (1995). These are empirically derived from algal populations measured at mid-latitudes under favourable algal growth conditions e.g. in the Atlantic Ocean, with 0.017 < [chl *a*] < 4.8 mg m^{-3}, and in the Mediterranean Sea where 0.06 <[chl *a*]< 7.5 mg m^{-3}. They may represent some c_i variability e.g. in different species present in the samples, but they are not representative of the variability in c_i and consequent flattening of $a^*_\Phi(\lambda)$ that results from pigment packaging induced by the high levels of physiological stress experienced by SO phytoplankton. The QAA $a^*_\Phi(\lambda)$ is chosen for satellite-derived [chl *a*], which is known to underestimate [chl *a*] in the polar SO (Kahru *et al.*, 2010), thereby selecting a more elevated $a^*_\Phi(\lambda)$ than would be appropriate for a measured [chl *a*] in the first instance, and then makes no adjustment for the flattening effects on $a^*_\Phi(\lambda)$ of photoacclimation. These two missteps result in an elevated $a^*_\Phi(\lambda)$, that is not appropriate for the region or the season. Zheng *et al.*, (2014) also found errors in the partitioning of absorption at high latitudes.

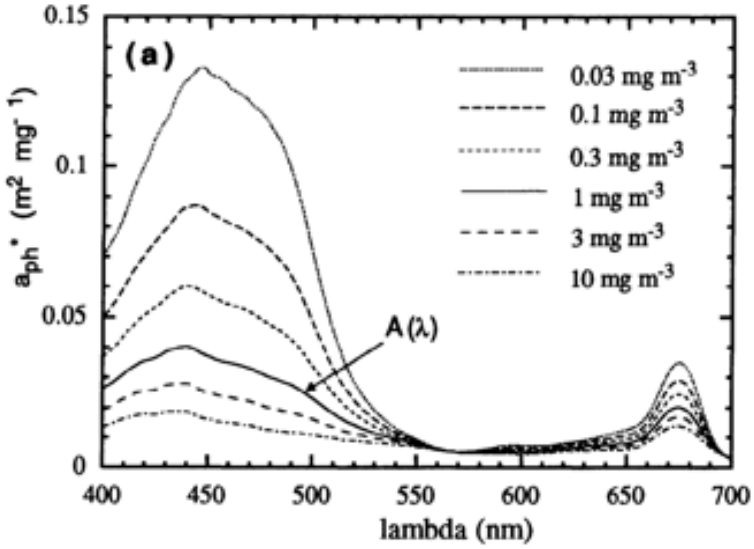

Figure 18: Figure 7a) from Bricaud et al., (1995) depicting $a^*_\Phi(\lambda)$ for different values of [chl a] concentration between 0.03 to 10 mg m^{-3}.

With known [chl *a*] and D_{eff}, and having demonstrated the impacts of physiology in Section 3.1.3, it is clear that the lack of adjustment of the reference $a^*_\phi(\lambda)$ for the optical effects of physiological changes driven by photoacclimation, is driving the overestimation of the OC-CCI $a_\phi(\lambda)$ product. This is compounded by the observed underestimation of [chl *a*] from the blended OC-CCI chl a product.

Conversely, choosing a Bricaud $a^*_\Phi(\lambda)$ to match a "depressed" SO $a^*_\Phi(\lambda)$ forces the selection of an unrealistically high [chl *a*] and/or an unrealistically large cell size, following the explanation of "the package effect" presented in Section 3.1.3.

Therefore it can be concluded that the primary driver of the depressed magnitude of SO $a_\Phi(\lambda)$ - which distinguishes it from other oceans - is pigment packaging as a photoacclimation response to low light conditions.

3.2. Addressing Aim 2: The Impact of Photoacclimation on Phytoplankton Backscatter

Having determined that photoacclimation has a significant impact on the magnitude of SO $a^*_{\Phi}(\lambda)$, the next step is to determine whether, or how, the resulting increased pigment density impacts upon $b^*_{b\Phi}(\lambda)$. It has been shown above that the EAP model, when parameterised appropriately for the seasonal growth conditions of the SO and constrained by measured [chl *a*] and D_{eff}, can approximately reproduce the corresponding measured $a_{\Phi}(\lambda)$ *and* $a^*_{\Phi}(\lambda)$. Given the biophysical consistency of particle optical properties in the EAP model (Lain *et al*., 2014), and previous radiometric validations of the phytoplankton-dominated waters of the Southern Benguela, one can assume some confidence in the corresponding modelled $b_{b\Phi}(\lambda)$ and $b^*_{b\Phi}(\lambda)$ (Lain *et al*., 2014). This is important for being able to look into the contribution of phytoplankton to the bulk optical signal.

The OC-CCI satellite $b_{bp}(\lambda)$ product describes the backscattering coefficient for the total in-water particulate assemblage (i.e. algal and non-algal). The spectral shape employed is a very generalised approximation described by Lee *et al*. (2009) as a log-normal distribution. *In situ* $b_{bp}(\lambda)$ data in the SO is limited, and *in situ* $b_{b\Phi}(\lambda)$ data even more so. The primary focus of this investigation is on the magnitude of the OC-CCI satellite $b_{bp}(\lambda)$ product rather than its spectral features, and more specifically the proportional contribution of $b_{b\Phi}(\lambda)$ as described by the model, to the magnitude of $b_{bp}(\lambda)$.

While there may be some concerns about the appropriateness of the absorption data products for use in the SO due to the assumption of Bricaud-like spectral shapes for $a^*_{\Phi}(\lambda)$, the same concerns need not apply to the $b_{bp}(\lambda)$ product, which is initially retrieved from the decomposition of the R_{rs} signal at 443 nm as previously mentioned in Section 2.3. Despite the imposition of an inappropriate spectral shape on $a^*_{\Phi}(\lambda)$, the magnitude of $a^*_{\Phi}(443)$, is less prone to large relative errors. The log-normal shape is simply applied to the statistically selected $b_{bp}(443)$. Therefore any $a^*_{\Phi}(\lambda)$-related assumptions that may not hold in the SO should not dramatically affect the retrieval of $b_{bp}(\lambda)$. According to Pitarch *et al*. (2019), data showed a bias of about 2.5-8.8 % for the QAA-derived $b_{bp}(\lambda)$ in Arctic waters, based on *in situ* matchups.

Modelled $b_{b\Phi}(\lambda)$ using the same [chl *a*], D_{eff} and c_i as per summer (5 kg m^{-3}) and winter (12 kg m^{-3}) models of $a_{\Phi}(\lambda)$, are compared to $b_{bp}(\lambda)$ retrieved from satellite. This allows us to determine the portion of $b_{bp}(\lambda)$ that can be attributed to phytoplankton at each station.

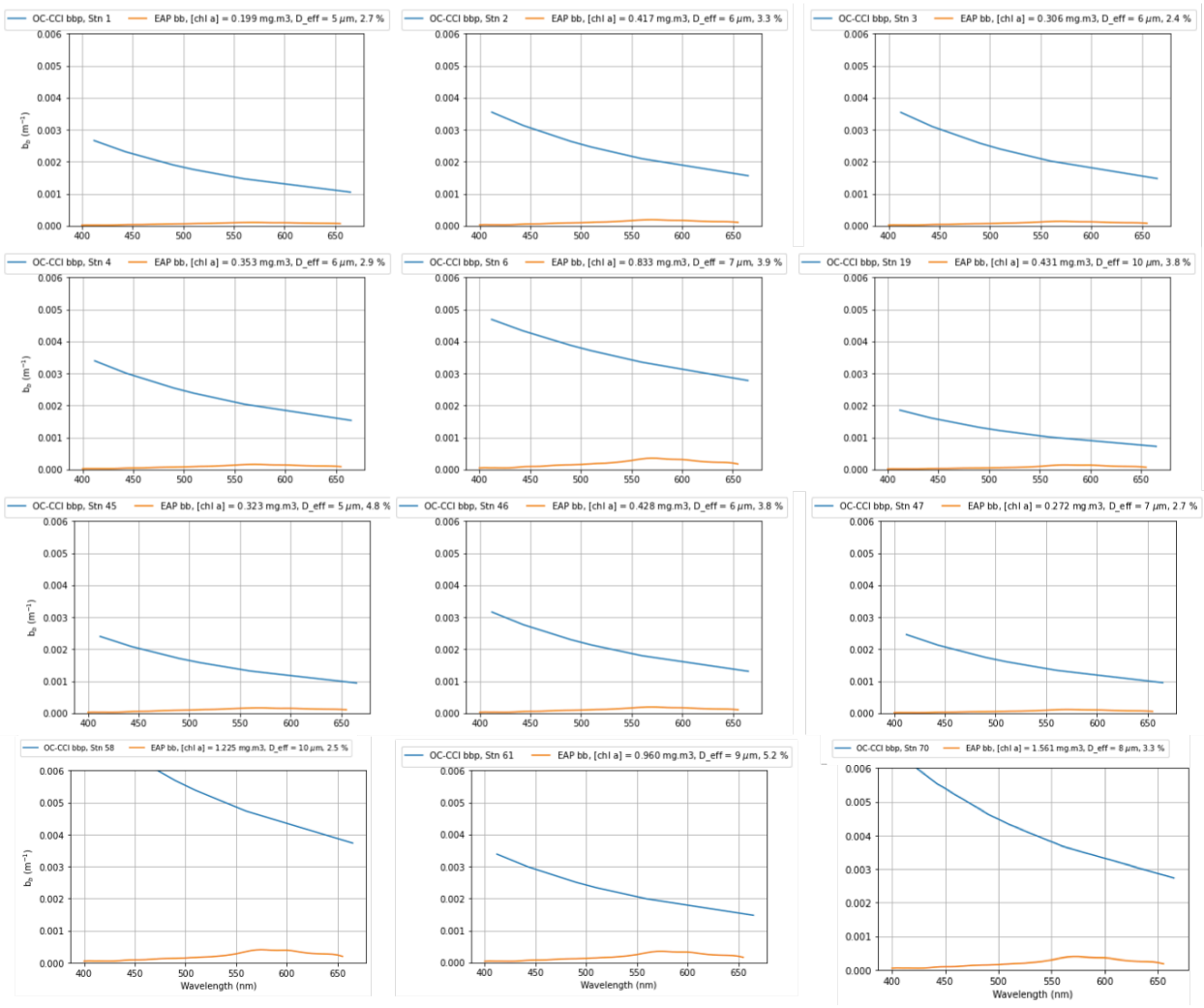

Figure 19: Summer satellite total $b_{bp}(\lambda)$, compared to the corresponding modelled $b_{b\Phi}(\lambda)$ for the same stations, including the proportional contribution of $b_{b\Phi}(\lambda)$ to total $b_{bp}(\lambda)$, calculated as difference in averages.

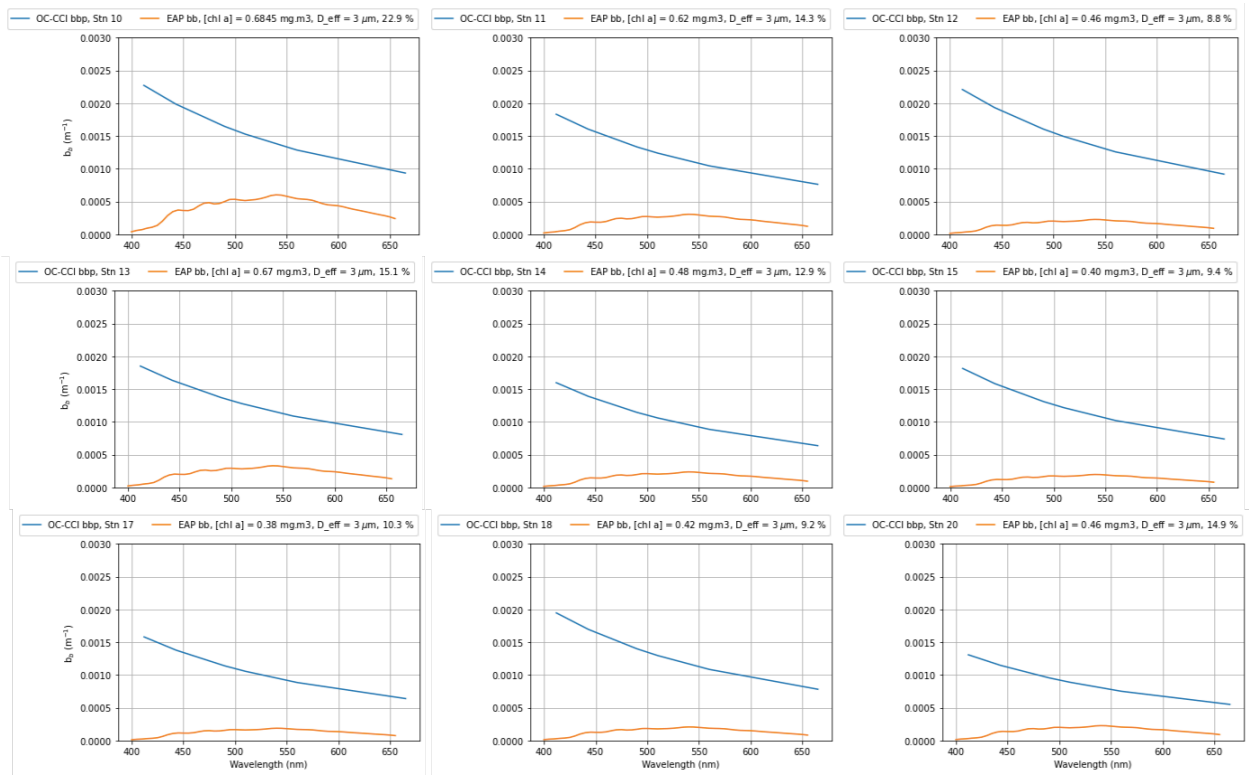

Figure 20: Winter satellite total $b_{bp}(\lambda)$, compared to the corresponding modelled $b_{b\Phi}(\lambda)$ for the same stations, including the proportional contribution of $b_{b\Phi}(\lambda)$ to total $b_{bp}(\lambda)$, calculated as differences in averages.

The magnitude of both summer (Fig. 19); and winter (Fig. 20) *in situ* $b_{b\Phi}(\lambda)$ is small in comparison to the total particulate satellite $b_{bp}(\lambda)$ (with a range of 2.4 - 5.2 % and 8.8- 22.9 % for summer and winter respectively). Although a slightly larger percentage contribution of $b_{b\Phi}(\lambda)$ to $b_{bp}(\lambda)$ was observed in winter, the total $b_{bp}(\lambda)$ was very small making it challenging to extract any signal with confidence. The higher proportion of phytoplankton $b_{b\Phi}(\lambda)$ to total $b_{bp}(\lambda)$ in winter may also be influenced by the lower biomass and an implied decline in detritus and therefore less $b_{bNAP}(\lambda)$ driving up the proportion of $b_{bp}(\lambda)$.

These observations fit with those previously reported by Bellacicco *et al*. (2018), who assert that an unusually large component of $b_{bNAP}(\lambda)$ which does not covary with [chl *a*], is found in the SO.

That being said, it has been shown above (Section 3.1.3) that SO phytoplankton are likely to have a higher pigment density than those in other oceans, possibly even in summer. The implication of this is that fewer cells are required to make up one unit of [chl *a*], and so the relationship between [chl *a*] and the volume of cells, or biomass, starts to break down. As such, in the SO, there is often a lower concentration of phytoplankton (biomass) than that

suggested by [chl *a*], when compared to other regions. This in itself has consequences for $b^*_{b\Phi}(\lambda)$, because fewer cells make up one unit of chl *a* than they do in other environments. These effects are articulated further in Fig. 21.

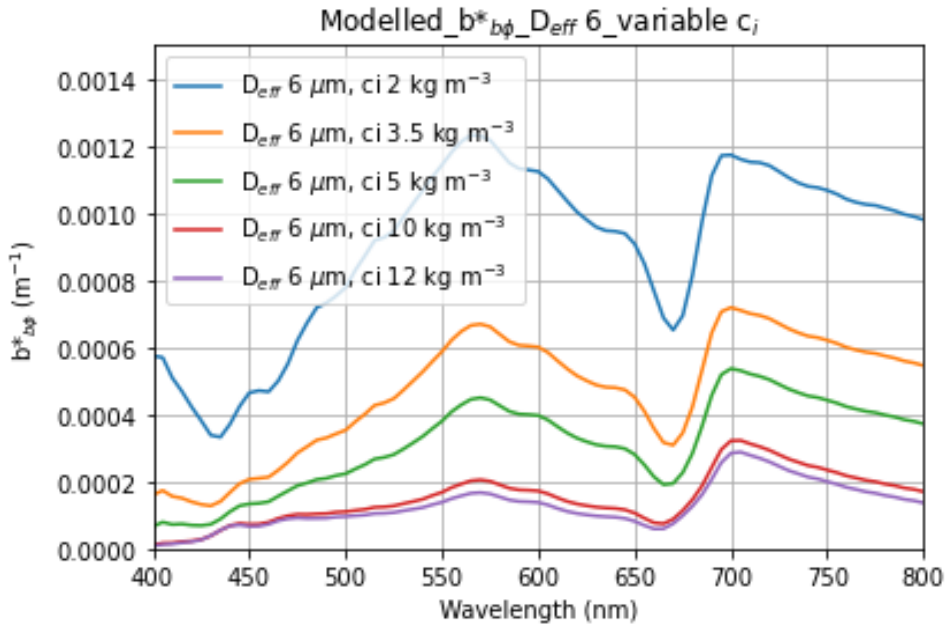

Figure 21: Modelled phytoplankton $b^*_{b\Phi}(\lambda)$ with a constant D_{eff} (6 µm) but a changing c_i ranging from 2 to 12 kg m^{-3}.

It is well known that $b^*_{b\Phi}(\lambda)$ increases as cell size decreases (eg. Lain *et al.*, 2014). Fig. 21 shows that for a given D_{eff}, $b^*_{b\Phi}(\lambda)$, also increases as c_i decreases. Thus, despite winter phytoplankton assemblages comprising primarily small cell sizes (3 and 4 µm), $b^*_{b\Phi}(\lambda)$, remains small because the c_i is particularly high due to photoacclimation. This is compounded by low *in situ* [chl *a*].

A re-interpretation of the measurements of Bellacicco *et al.*, (2018), may be useful: $b_{b\Phi}(\lambda)$ is lower in the SO, but the accompanying detrital backscattering, $b_{bDET}(\lambda)$, will be proportionally higher as those particles do not photoacclimate. They may covary in particle volume, while not in their optical signals. This would address some of the unusual and unexplained observations of a disproportionally high $b_{bNAP}(\lambda)$ in the SO.

In addition to the simple matter of a unit of a [chl *a*] comprising fewer cells, it is likely that there is an increase in the magnitude of the imaginary refractive index with increased pigment density. This has implications for the magnitude of the real refractive index, which then tends to decrease (D. Stramski, *pers comm*). This is expressed in the optics as a reduction in the cross-sectional backscattering efficiency of each cell. The latter reason for

reduced backscatter is not represented in the model and so we cannot quantify its effects. In nature these two effects work together to contribute to even less overall $b_{b\Phi}(\lambda)$ as c_i increases, than is shown by the model.

3.3. Addressing Aim 3: Implications for Carbon Estimates from Satellite

In this Section the implications for satellite POC retrievals, will be discussed. It has been shown above that there is very little $b_{b\Phi}(\lambda)$ in comparison to $b_{bp}(\lambda)$ in the SO. Intuitively, this suggests that the determination of phytoplankton POC (C_{phyto}) from $b_{bp}(\lambda)$ would be very challenging. This suggestion is discussed and then contextualised against $b_{b\Phi}(\lambda)$ signals in a growth favourable region.

$b_{b\Phi}(\lambda)$ is understood to be related to cellular carbon content (Stramski, 1997). The real part of the refractive index is linked to the physical and chemical composition of the material, absorbs very little, and has been shown to correlate well with the intracellular concentration of carbon, C_i (Stramski 1999). With the assumption that a similar relationship applies to non-algal particulate, many algorithms exploit this observation either directly or indirectly (avoiding quantification of the real refractive index) by describing a relationship between $b_{bp}(\lambda)$ and POC.

In more temperate oceans, many promising relationships have been explored. For example, Graff *et al*., (2015) found a strong relationship between C_{phyto} and $b_{bp}(\lambda)$ in diverse regions, ranging from the Pacific and Atlantic oligotrophic gyres to equatorial upwelling systems and temperate spring conditions. From the same study (Graff *et al*., 2015), there has also been a relationship found between [chl *a*] and total POC concentration, but it is not as well defined. However, there are demonstrated concerns about the decoupling of C_{phyto} and $b_{bp}(\lambda)$ in regions with high $b_{bDET}(\lambda)$, and also of [chl *a*] and biomass. A better understanding of these relationships in the SO is thus needed.

Martinez-Vincente et al., 2017 investigate six ocean color algorithms by comparison with *in situ* estimates of C_{phyto}. The algorithms are broadly classified into three classes: chlorophyll-based, back-scattering based and allometric. It is noted that there is no significant difference in performance between the selected approaches when the entire matchup dataset is used, although there are differences in performance when the matchup dataset is redacted into water class types. Again, the matchup dataset is grossly undersampled in the Southern Ocean, especially in the Atlantic sector where this study takes place.

3.3.1. Pursuing Phytoplankton Carbon from $b_{bp}(\lambda)$

Based on the small proportional contribution of phytoplankton to total backscatter (in particular in summer) and no clear quantification of biomass in terms of cell volume when using [chl *a*] as an indication of phytoplankton concentration rather than pigment concentration, it appears to be clear that the determination of C_{phyto} from $b_{b\Phi}(\lambda)$ (or even as a portion of $b_{bp}(\lambda)$) is not an appropriate method for the SO.

To contextualise the SO $b_{b\Phi}(\lambda)$ contribution to $b_{bp}(\lambda)$, some data from the lower latitude Southern Benguela is presented for comparison. The Southern Benguela coastal region is not considered light or nutrient limited in general circumstances. In addition, the consistent availability of bright sunlight implies no strong demand for phytoplankton to have to photoacclimate.

The $a_{\Phi}(\lambda)$ here (Fig. 22(a)) was modelled in the same way as in Section 3.1 summer and winter plots, using the *in situ* measured D_{eff} (8 µm) and [chl *a*] (43 mg m^{-3}) and a best fit c_i (of 3.5 kg m^{-3}). The absence of photoacclimation issues is clear with both the modelled $a_{\Phi}(\lambda)$ and measured $a_{\Phi}(\lambda)$ being the same order of magnitude as the satellite OC-CCI derived $a_{\Phi}(\lambda)$ (i.e. with no observed flattening of the *in situ* spectra). The effect of a low c_i together with very high biomass is clearly demonstrated in Fig. 22(b), with a much larger proportion of the total $b_{bp}(\lambda)$ being due to phytoplankton, contributing up to ~50 % , or more, depending on which wavelength one is looking at (with an average contribution across the 5 wavelengths of 33.1 %).

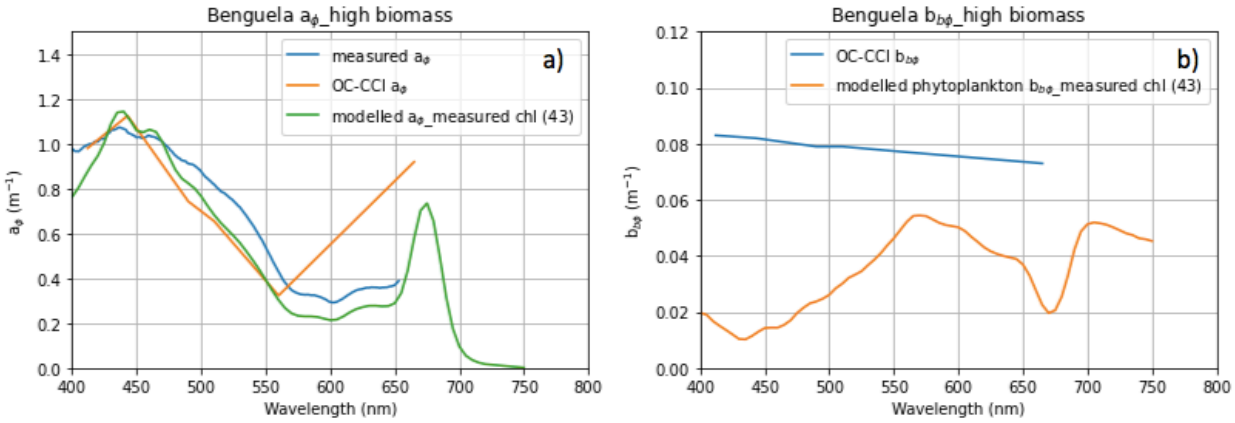

Figure 22: An example of high biomass bloom conditions from the lower latitude Benguela upwelling system showing a) the in situ measured absorption (blue), the satellite $a_{\Phi}(\lambda)$ (orange) and the modelled $a_{\Phi}(\lambda)$ from in situ [chl a] of 43 mg m^{-3} (green) and b) the total satellite derived $b_{bp}(\lambda)$ (blue) and the modelled $b_{b\Phi}(\lambda)$ from in situ [chl a] of 43 mg m^{-3} (orange).

A similar scenario was evident when a much lower biomass station of 1.4 mg m^{-3} was considered for the low latitude Benguela (Fig. 23(b)). Again, both the modelled and measured $a_{\Phi}(\lambda)$ were of the same order of magnitude as the satellite derived $a_{\Phi}(\lambda)$. In addition, the $b_{b\Phi}(\lambda)$ still comprises a substantial proportion (20.3 %) of the total $b_{bp}(\lambda)$, when compared to the SO in summer (2.4 - 5.2 %) and at the upper limit of what was observed in the SO in winter (8.8- 22.9 %).

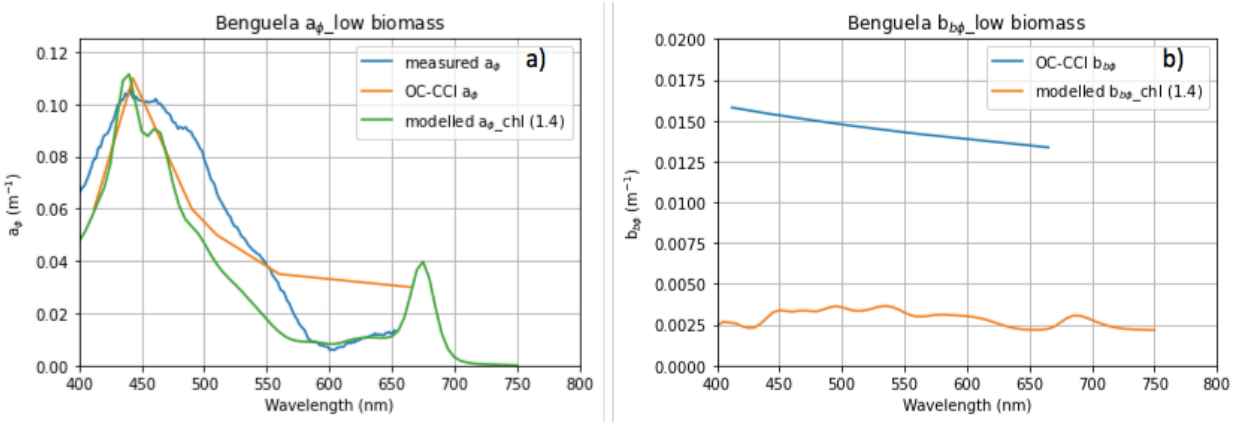

Figure 23: a) An example of low biomass conditions from the lower latitude Benguela upwelling system showing a) the in situ measured absorption (blue), the satellite $a_{\Phi}(\lambda)$ (orange) and the modelled $a_{\Phi}(\lambda)$ from in situ [chl a] of 1.4 mg m^{-3} (green) and b) the total satellite derived $b_{bp}(\lambda)$ (blue) and the modelled $b_{b\Phi}(\lambda)$ from the in situ [chl a] of 1.4 mg m^{-3} (orange).

The proportional signal of $b_{b\Phi}(\lambda)$ to $b_{bp}(\lambda)$ are not well described, but are known to vary between different oceans (Dall'olmo 2009). In the high biomass Benguela conditions, one would expect the $b_{b\Phi}(\lambda)$ signal to be large, because there are so many cells present. This lends itself well to C_{phyto} quantification in the context of the total $b_{bp}(\lambda)$ signal. One may even be able to spot changes in $b_{bp}(\lambda)$ due to changes in $b_{b\Phi}(\lambda)$ and most likely derive some quantifiable relationship between the proportion of $b_{bp}(\lambda)$ and $b_{b\Phi}(\lambda)$. The low biomass example is not quite as impressive, but still, the total signal in $b_{bp}(\lambda)$ was sufficiently high (unlike in winter in the SO) with a substantial proportion of total $b_{bp}(\lambda)$ coming from phytoplankton. This is however evidently not the case in the SO either in winter, where the total $b_{bp}(\lambda)$ signal was too low (despite an increase in the proportion of $b_{b\Phi}(\lambda)$), and in summer, where the contribution of $b_{b\Phi}(\lambda)$ to total $b_{bp}(\lambda)$ was typically <5 %.

3.3.2. Pursuing POC from Particulate Size Distributions

Some algorithms focus on the retrieval of a PSD from a power law particle size spectrum from satellite ocean colour observations (Kostadinov 2009, 2012), and calculate POC accordingly (Kostadinov *et al.*, 2022). Unfortunately, a further implication of reduced

$b^*_{b\Phi}(\lambda)$ is that the relationship between backscatter and particle size, so well established in Mie theory, falls apart at very small sizes and very high c_i.

This is elaborated in Fig. 24 where $b^*_{b\Phi}(\lambda)$ is modelled for two size classes (3 and 6 µm) and three c_i's (2, 5 and 12 kg m^{-3}). Here a D_{eff} of 3 µm with a c_i of 12 kg m^{-3}, represents a small celled community in very low light (i.e. a typical SO winter assemblage). Whereas a D_{eff} of 6 µm with a c_i of 2 kg m^{-3}, represents a larger celled community in high light (i.e. a typical Benguela summer assemblage). Fig. 24 shows that the highest $b^*_{b\Phi}(\lambda)$ is observed with small cells and no acclimation (c_i = 2 kg m^{-3}). It also shows that the lowest $b^*_{b\Phi}(\lambda)$ is observed with larger cells and strong acclimation (c_i = 12 kg m^{-3}). Smaller cells with less/ no acclimation results in the highest $b^*_{b\Phi}(\lambda)$. The $b^*_{b\Phi}(\lambda)$ in the SO is typically low.

This affects the interpretation of PSD retrievals from $b^*_{b\Phi}(\square)$. Fig. 24 makes clear that $b^*_{b\Phi}(\lambda)$ is not necessarily a reliable indicator of PSD for the phytoplankton portion of $b_{bp}(\lambda)$ if changes in photoacclimation via cellular adjustments in c_i are not taken into consideration.

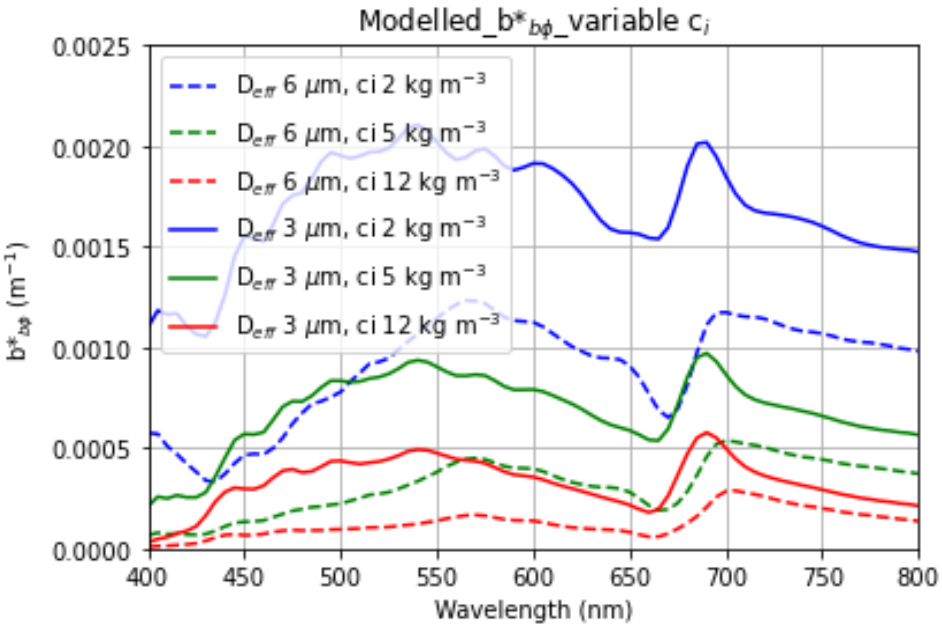

Figure 24: Modelled $b^*_{b\Phi}(\lambda)$ for D_{eff} of 3 µm and 6 µm, with variable c_i of 2, 5 and 12 kg m^{-3}.

Stramski (1999) describes a relationship between cellular real refractive index and cellular carbon content. While in nature the refractive index of each phytoplankton cell changes with variability in c_i, this is not dealt with explicitly in the model. Small changes in the real refractive index and consequent uncertainty in cellular carbon content is therefore not accounted for. This approach (Stramski 1999) to quantifying phytoplankton carbon in a

population also requires the particle volumes to be known, returning to the problem of PSD retrieval.

3.3.3. Careful Considerations Towards Parameterisation of a New C_{phyto} Approach

For the reasons outlined above, the determination of C_{phyto} directly from satellite backscatter products or indirectly from satellite POC products in the SO likely requires a new approach, or amendments to current methods to incorporate the understanding of how photoacclimation affects bio optics. One approach could possibly be to adjust the OC-CCI data products, notably the $a_{\Phi}(\lambda)$, with a seasonal and/or latitudinal "correction factor", to address and account for c_i changes and therefore a re-interpretation of bio optics in the SO. If assemblage information is retrievable from satellite $a_{\Phi}(\lambda)$, the corresponding IOPs could be modelled, and biogeochemical quantities like POC could be inferred.

The combined optical impacts of community structure adjustments and photophysiological changes occur continuously and simultaneously in natural assemblages over time and space. Attempting to uniquely infer either assemblage structure or physiological information from satellite derived $a_{\Phi}(\lambda)$ spectra is thus not appropriate where D_{eff} and c_i cannot be estimated with confidence.

The potential for ambiguity in the interpretation of the phytoplankton IOPs $b^*_{b\Phi}(\lambda)$ signal composition if D_{eff} and/or c_i is not known is highlighted in Fig. 24, where a reduction in D_{eff} and a reduction in c_i both independently drive higher $b^*_{b\Phi}(\lambda)$. This leads to the important observation that the phytoplankton size vs $b^*_{b\Phi}(\lambda)$ relationship falls away when photoacclimation is at play.

In order for the EAP model to appropriately reproduce phytoplankton optical properties, the assemblage descriptors used as inputs to the model need to be precise. For example, although [chl *a*] concentration can be readily determined both *in situ* and from satellite, differences between the two are common for the SO with implications for IOPs. Phytoplankton assemblage D_{eff} is not yet reliably retrieved from radiometry in low biomass, but can be measured *in situ* with some provisos - notably that particle sizers do not generally distinguish between algal and non-algal particles. In addition, they generally constitute a specific size window with the possibility of excluding particles smaller or larger than the specified size window. Sorting cytometry would be better for characterising the different particle assemblages, while a combination of different size windows (e.g. from the combination of a flow cytometer and a Coulter counter) would be better for capturing the full size spectrum of the particle field. Although c_i is not routinely measured,

it can be calculated from [chl *a*] divided by the volume of algal cells - and is therefore subject to the same uncertainty as the D_{eff} parameter.

There is ongoing work being conducted, such as Bellacicco *et al*., (2020), to improve the retrieval of carbon-based phytoplankton biomass from satellite ocean colour observations. An algorithm by Bellacicco *et al*., 2020 to determine phytoplankton C from space was developed. It takes into consideration spatio-temporal variations of the backscattering coefficients that is related to the fraction of detrital particles that do not covary with [chl a] (although not addressing any difference between [chl a] and phytoplankton concentration, as discussed in Section 3.3.1). Other work in improving our understanding of retrieving carbon from satellites has been conducted, such as: Bellacicco *et al*., (2016), Behrenfeld *et al*., (2005), Loisel *et al*., (2018), Sathyendranath *et al*., (2017), Martinez-Vincente *et al*., 2017 and Evers-King *et al*., 2017.

Evers-King et al., 2017 investigates a number of algorithms to derive POC using different optical variables that are applied to merged satellite OC-CCI ocean color data and validated against the largest database of *in situ* POC measurements currently available. This study observes that regionally specific algorithms frequently outperform generalised ones, and that the blending of region-specific algorithms may provide the best way forward for generating global POC products.

Currently, the OC-CCI data products do not account for the optical effects of photophysiological changes on phytoplankton IOPs. The methods by which the OC-CCI satellite data products are obtained from algorithms rely heavily on parameterisation using datasets not representative of SO conditions including the very light variable and often light limited environment, resulting in an insufficiently broad range of photophysiology-driven ci variability. The flattening effects of photoacclimation and increased c_i on the $a_{\Phi}(\lambda)$ are therefore not properly represented in the OC-CCI data products.

As a consequence of increased c_i, the model indicates a previously unquantified reduction of $b_{b\Phi}(\lambda)$. This may indicate unexpected variability in the contribution of C_{phyto} to $b_{bp}(\lambda)$,and full parameterisation of these changes may inform on the potential for improving retrievals of assemblage and growth information from satellite-derived IOPs in future.

Chapter 4

4. Conclusions and Recommendations

Being able to retrieve optical properties of SO phytoplankton from space and accurately converting them into valid biological quantities will aid our understanding of the current and future role of the BCP. SO phytoplankton have unique optical properties when compared to other oceans, displaying a characteristically "depressed" absorption spectra. The primary aim of this study is to better understand the causal drivers of the optical differentiation of SO $a^*_{\Phi}(\lambda)$ spectra and to determine if there is a corresponding impact on $b^*_{b\Phi}(\lambda)$ and what the implications of this understanding is on satellite retrievals of both $a^*_{\Phi}(\lambda)$, $b^*_{b\Phi}(\lambda)$ as well as POC.

From the study, it can be concluded that when D_{eff} is properly accounted for, physiological adaptations due to photoacclimation likely drive the observed variability in the magnitude (flattening) of SO $a_{\Phi}(\lambda)$ and $a^*_{\Phi}(\lambda)$ spectra.

Photoacclimation was also shown to impact on $b^*_{b\Phi}(\lambda)$, significantly reducing it under low light conditions. As a result, the cell size/$b_{b\Phi}(\lambda)$ relationship does not always hold in the SO conditions and phytoplankton physiology becomes an essential part of the optical puzzle. SO phytoplankton have very unique photophysiological response strategies to their extreme environment (Ryan-Keogh *et al*., submitted 2022) and these need to be properly understood and optically characterised if we are to be able to correctly interpret SO IOPs.

The impacts of photoacclimation on $b_{b\Phi}(\lambda)$ and consequently $b_{bp}(\lambda)$ has serious implications for the estimation of C_{phyto} from total $b_{bp}(\lambda)$ derived by satellite inversion algorithms, and widely used in climate models. Relying on an identifiable $b_{b\Phi}(\lambda)$ contribution to the $b_{bp}(\lambda)$ signal to quantify C_{phyto} is not a robust approach in the SO, with experiments in Section 3.2 showing how little $b_{b\Phi}(\lambda)$ impacts upon total $b_{bp}(\lambda)$ signal. In addition, any relationship to POC or C_{phyto} derived from the bulk backscatter $b_{bp}(\lambda)$ relies on some predictable relationship between the concentrations of phytoplankton and detrital particle concentrations. However, covariability between the detrital and phytoplankton components is not well understood in the SO (Bellacicco *et al*., 2018) and this also impacts upon POC retrievals.

The difficulty in estimating C_{phyto} from $b_{b\Phi}(\lambda)$ (as was observed for the SO) may however not apply in other regions. For example when looking into the low latitude high biomass

Benguela upwelling system (where neither light nor nutrients is expected to be limiting) we see that phytoplankton $b_{b\Phi}(\lambda)$ comprises a large portion of the total $b_{bp}(\lambda)$ signal. In this instance it is more plausible to be able to extract a proxy for C_{phyto} from satellite $b_{bp}(\lambda)$.

A new approach to retrieving accurate biogeochemical properties from ocean colour R_{rs} may be to improve satellite derived absorption products, facilitating better parameterisation of phytoplankton community structure and growth limitations and the use of modelling to estimate the corresponding $b_{b\Phi}(\lambda)$ for those assemblages.

A new understanding of phytoplankton biomass in the SO is also needed as [chl a] is not an accurate predictor of the volume of phytoplankton cells (given that it can change independently with pigment packaging). Finally, the relationships between [chl a], C_{phyto} and detrital concentration should be further studied, as proportional relationships in terms of concentrations (particle numbers) and respective contribution to backscatter, are needed for POC solutions.

In the SO, it is shown that seasonal variability in c_i can vary by more than 100%. This study is the first to our knowledge to approximately quantify the variability in phytoplankton IOPs (and their proportional contribution to the total IOPs) induced by photoacclimation-driven changes in cellular photophysiology. We describe how photoacclimation effects can lead to significant ambiguity if the interpretation of $a^*_{\Phi}(\lambda)$ is primarily cell size-driven, with a ten-fold error in cell size being possible if c_i variability is not acknowledged. The corresponding impact on phytoplankton backscatter similarly shows a reduction in signal as c_i increases, and we demonstrate the potential for causal ambiguity in phytoplankton IOPs between the effects of cell size and c_i . These findings raise concerns for the derivation of PSD from $b_{bp}(\lambda)$ and further, for the derivation of $b^*_{b\Phi}(\lambda)$ from $b_{bp}(\lambda)$.

Bio-optical parameterisations not specifically tailored for the SO can result in low confidence in the retrieval of [chl *a*] from datasets employing generalised algorithms. The two primary chl a algorithms used for the SO OC CCI data in this study are OCI and OC5. These are parameterised with the NOMAD dataset and validated with the Valente dataset, both of which are heavily biased towards the lower latitudes in the Southern Hemisphere. This results in an implied overestimation of phytoplankton cell size because the effects of photoacclimation on $a^*_{\Phi}(\lambda)$ are neglected and an allometric relationship between cell size and [chl a] - appropriate for lower latitudes and more favourable growth conditions - is assumed.

It is acknowledged that there are shortcomings in the methodologies used in this study, particularly the lack of particle size data <2 um, and the lack of validation of OC-CCI satellite $b_{bp}(\lambda)$.

5. References

[1] Schlitzer, R. (2002). Carbon export fluxes in the Southern Ocean: results from inverse modeling and comparison with satellite-based estimates., Deep Sea Research Part II: Topical Studies in Oceanography, 49(9-10), 1623-1644.

[2] Dall'Olmo, G., et al. (2011). Inferring phytoplankton carbon and eco- physiological rates from diel cycles of spectral particulate beam-attenuation coefficient., Biogeosciences, 8.11: 3423-3439.

[3] Sarmiento, J.L. and Gruber, N. (2002). Sinks for anthropogenic carbon., Physics today: 30-36.

[4] Finkel, Z. V., Beardall, J., Flynn, K. J., Quigg, A., Rees, T. A. V., and Raven, J. A. (2010). Phytoplankton in a changing world: cell size and elemental stoichiometry., Journal of plankton research, 32(1), 119-137.

[5] Winder, M. and Sommer, U., (2012). Phytoplankton response to a changing climate., Hydrobiologia., 698.1: 5-16. science, 316.5832: 1735-1738.

[6] Le Quéré, C., Rodenbeck, C., Buitenhuis, E.T., Conway, T.J., Langenfelds, R., Gomez, A., Labuschagne, C., Ramonet, M., Nakazawa, T., Metzl, N. and Gillett, N., (2007). Saturation of the Southern Ocean CO2 sink due to recent climate change., science., 316.5832: 1735-1738.

[7] Matear, R.J. and Hirst, A.C., (1999). Climate change feedback on the future oceanic CO2 uptake., Tellus., B 51.3: 722-733.

[8] Chisholm, S. W. (1992). Phytoplankton size. In Primary productivity and biogeochemical cycles in the sea., Springer, Boston, MA., pp. 213-237.

[9] Munk, W. H. (1952). Absorption of nutrients by aquatic plants., J. mar. Res., 11, 215-240.

[10] Parsons, T. R., and M. Takahashi. (1973). Environmental control of phytoplankton cell size., Limnology and Oceanography, 18.4: 511-515.

[11] Semina, H. J. (1972). The size of phytoplankton cells in the Pacific Ocean., Internationale Revue der gesamten Hydrobiologie und Hydrographie., 57.2: 177- 205.

[12] IOCCG, (2014). Phytoplankton Functional Types from Space. Sathyendranath, S. (ed.)., Reports of the International Ocean-Colour Coordinating Group, No. 15, IOCCG, Dartmouth, Canada.

[13] Bienfang, P.K. and Harrison, P.J., (1984). Co-variation of sinking rate and cell quota among nutrient replete marine phytoplankton., Mar. Ecol. Prog. Ser, 14, pp.297-300.

[14] Stemmann, L. and Boss, E., (2012). Plankton and particle size and packaging: from determining optical properties to driving the biological pump., Annual Review of Marine Science, 4, pp.263-290.

[15] Kahru, M. and Mitchell, B.G., (2010). Blending of ocean colour algorithms applied to the Southern Ocean., Remote Sensing Letters, 1.2: 119-124.

[16] Kirk, J. T. O., (1994). Light and Photosynthesis in Aquatic Ecosystems., Cambridge Univ. Press, New York, 509 pp.

[17] Cox, P.M., Betts, R.A., Jones, C.D., Spall, S.A. and Totterdell, I.J., (2000). Acceleration of global warming due to carbon- cycle feedbacks in a coupled climate model., Nature, 408.6809: 184-187.

[18] Orr, J.C., Fabry, V.J., Aumont, O., Bopp, L., Doney, S.C., Feely, R.A., Gnanadesikan, A., Gruber, N., Ishida, A., Joos, F. and Key, R.M., (2005). Anthropogenic ocean acidification over the twenty-first century and its impact on calcifying organisms. Nature, 437.7059: 681-686.

[19] A. Morel, (Academic, 1974). Optical properties of pure seawater. Optical As- pects of Oceanography, N. G. Jerlov and E. S. Nielsen, eds., pp. 1–24.

[20] Gibson, R.N., Atkinson, R.J.A. and Gordon, J.D.M., (2007). Inherent optical properties of non-spherical marine-like particles from theory to observation. Oceanogr Mar Biol., 45, pp.1-38.

[21] Vaillancourt, R.D., Brown, C.W., Guillard, R.R. and Balch, W.M., (2004). Light backscattering properties of marine phytoplankton: relationships to cell size, chemical composition and taxonomy. Journal of plankton research, 26.2: 191-212.

[22] Mobley, C.D. and Mobley, C.D., (1994). Light and water: radiative transfer in natural waters. Academic press.

[23] Talley, L.D. et al, (2011). Descriptive physical oceanography: an introduction. Academic press.

[24] Kostadinov, T.S., Siegel, D.A. and Maritorena, S., (2009). Retrieval of the particle size distribution from satellite ocean color observations. Journal of Geophysical Research: Oceans, 114(C9).

[25] Neukermans, G., Loisel, H., M´eriaux, X., Astoreca, R. and McKee, D., (2012). In situ variability of mass-specific beam attenuation and backscattering of ma- rine particles with respect to particle size, density, and composition. Limnology and Oceanography, 57(1),

pp.124-144.

[26] Ulloa, O., Sathyendranath, S. and Platt, T., (1994). Effect of the particle-size distribution on the backscattering ratio in seawater. Applied Optics, 33(30), pp.7070-7077.

[27] Dall'Olmo, G., Westberry, T.K., Behrenfeld, M.J., Boss, E. and Slade, W.H., (2009). Significant contribution of large particles to optical backscattering in the open ocean. Biogeosciences, 6.6: 947-967.

[28] Organelli, E., Dall'Olmo, G., Brewin, R.J., Nencioli, F. and Tarran, G.A., (2020). Drivers of spectral optical scattering by particles in the upper 500 m of the Atlantic Ocean. Optics Express, 28.23: 34147-34166.

[29] Laiolo, L., Matear, R., Soja-Wo´zniak, M., Suggett, D.J., Hughes, D.J., Baird, M.E. and Doblin, M.A., (2021). Modelling the impact of phytoplankton cell size and abundance on inherent optical properties (IOPs) and a re- motely sensed chlorophyll-a product. Journal of Marine Systems, Volume 213: 103460.

[30] Bricaud, A., Claustre, H., Ras, J., and Oubelkheir, K. (2004). Natural variability of phytoplanktonic absorption in oceanic waters: Influence of the size struc- ture of algal populations., Journal of Geophysical Research: Oceans, 109(C11).

[31] Lain, L.R., Bernard, S. and Evers-King, H., (2014). Biophysical modelling of phytoplankton communities from first principles using two-layered spheres: Equivalent Algal Populations (EAP) model., Optics express, 22.14: 16745- 16758.

[32] Bricaud, A., B´edhomme, A.L. and Morel, A., 1988. Optical properties of diverse phytoplanktonic species: experimental results and theoretical interpre- tation., Journal of Plankton Research, 10(5), pp.851-873.

[33] Baird, M., Dutkiewicz, S., Hickman, A., Mongin, M., Soja-Wozniak, M., Sker- ratt, J. and Wild-Allen, K., (2022). Modeling phytoplankton processes in mul- tiple functional types., Advances in Phytoplankton Ecology, Elsevier. 245-264.

[34] Kopelevich, O., Burenkov, V., Sheberstov, S., Vazyulya, S., Kravchishina, M., Pautova, L., Silkin, V., Artemiev, V. and Grigoriev, A., (2014). Satellite monitoring of coccolithophore blooms in the Black Sea from ocean color data. Remote sensing of environment, 146: 113-123.

[35] Bricaud, A., B´edhomme, A.L. and Morel, A., (1988). Optical properties of di- verse phytoplanktonic species: experimental results and theoretical interpre- tation. Journal of Plankton Research, 10(5), pp.851-873.

[36] Graff, J.R., Westberry, T.K., Milligan, A.J., Brown, M.B., Olmo, G.D., Reifel, K.M. and Behrenfeld, M.J., (2016). Photoacclimation of natural phytoplankton communities. Marine

Ecology Progress Series, 542, pp.51-62.

[37] Behrenfeld, M.J. and Boss, E., (2003). The beam attenuation to chlorophyll ratio: an optical index of phytoplankton physiology in the surface ocean?. Deep Sea Research Part I: Oceanographic Research Papers, 50(12), pp.1537- 1549.

[38] Moore, C.M., Seeyave, S., Hickman, A.E., Allen, J.T., Lucas, M.I., Planquette, H., Pollard, R.T. and Poulton, A.J., (2007). Iron–light interactions during the CROZet natural iron bloom and EXport experiment (CROZEX) I: Phytoplankton growth and photophysiology. Deep Sea Research Part II: Topical Studies in Oceanography, 54(18-20), pp.2045-2065.

[39] Hassler, C.S., Sinoir, M., Clementson, L.A. and Butler, E.C., (2012). Exploring the link between micronutrients and phytoplankton in the Southern Ocean during the 2007 austral summer. Frontiers in Microbiology, 3, p.202.

[40] Bellacicco, M., Cornec, M., Organelli, E., Brewin, R.J.W., Neukermans, G., Volpe, G., Barbieux, M., Poteau, A., Schmechtig, C., d'Ortenzio, F. and Marullo, S., (2019). Global variability of optical backscattering by non-algal particles from a biogeochemical-Argo data set. Geophysical Research Letters, 46(16), pp.9767-9776.

[41] Sosik, H. M. (2008). Characterizing seawater constituents from optical properties. Real-time coastal observing systems for ecosystem dynamics and harmful algal blooms, edited by: Babin, M., Roesler, CS, and Cullen, JJ UNESCO, 281-329.

[42] Morel, A., (1988). Optical modeling of the upper ocean in relation to its biogenous matter content (case I waters). Journal of geophysical research: oceans, 93(C9), pp.10749-10768.

[43] Koestner, D. W. (2019). Measurements of angle-resolved polarized light scat- tering by seawater as a tool to characterize natural assemblages of marine particles. University of California, San Diego.

[44] Stramski, D., Boss, E., Bogucki, D. and Voss, K.J., (2004). The role of seawater constituents in light backscattering in the ocean. Progress in Oceanography, 61(1), pp.27-56.

[45] Szeto, M., Werdell, P.J., Moore, T.S. and Campbell, J.W., (2011). Are the world's oceans optically different?. Journal of Geophysical Research: Oceans, 116(C7).

[46] H. Dierssen, M. Vernet, and R. Smith, (2000). Optimizing models for remotely estimating primary production in antarctic coastal waters. Antarctic Sci., 12(1), 20–32.

[47] Garcia, C.A.E., Garcia, V.M.T. and McClain, C.R., (2005). Evaluation of SeaW- iFS chlorophyll algorithms in the Southwestern Atlantic and Southern Oceans. Remote Sensing of Environment, 95(1), pp.125-137.

[48] Mitchell, B.G. and Holm-Hansen, O., (1991). Bio-optical properties of Antarc- tic Peninsula waters: Differentiation from temperate ocean models. Deep Sea Research Part A. Oceanographic Research Papers, 38(8-9), pp.1009-1028.

[49] Mitchell, B.G. and Kahru, M., (2009). Bio-optical algorithms for ADEOS-2 GLI. Journal of The Remote Sensing Society of Japan, 29(1), pp.80-85.

[50] Robinson, C.M., Huot, Y., Schuback, N., Ryan-Keogh, T.J., Thomalla, S.J. and Antoine, D., (2021). High latitude Southern Ocean phytoplankton have distinctive bio-optical properties. Optics Express, 29(14), pp.21084-21112.

[51] Bellacicco, M., Volpe, G., Colella, S., Pitarch, J. and Santoleri, R., (2016). Influ- ence of photoacclimation on the phytoplankton seasonal cycle in the Mediter- ranean Sea as seen by satellite. Remote Sensing of Environment, 184, pp.595- 604.

[52] Halsey, K. H. and Jones, B. M., (2015). Phytoplankton strategies for photosynthetic energy allocation. Annu. Rev. Mar. Sci., 7, 265–297.

[53] Bellacicco, Marco, et al. (2018). Global distribution of non-algal particles from ocean color data and implications for phytoplankton biomass detection. Geo- physical Research Letters, 45.15: 7672-7682.

[54] Roy, S., Sathyendranath, S. and Platt, T., (2017). Size-partitioned phytoplankton carbon and carbon-to-chlorophyll ratio from ocean colour by an absorption-based bio-optical algorithm. Remote Sensing of Environment, 194, pp.177-189.

[55] Bernard, S., F. A. Shillington, and T. A. Probyn. (2007). The use of equivalent size distributions of natural phytoplankton assemblages for optical modeling. Optics express, 15.5: 1995-2007.

[56] Bernard, S., Probyn, T.A. and Quirantes, A., (2009). Simulating the optical properties of phytoplankton cells using a two-layered spherical geometry. Bio- geosciences Discussions, 6(1), pp.1497-1563.

[57] Stephens, F.C., (1995). Variability of spectral absorption efficiency within living cells of Pyrocystis lunula (Dinophyta). Marine Biology, 122(2), pp.325-33

[58] Zaneveld, J.R.V. and Kitchen, J.C., (1995). The variation in the inherent optical properties of phytoplankton near an absorption peak as determined by various models of cell structure. Journal of Geophysical Research: Oceans, 100(C7), pp.13309-13320.

[59] Bricaud, A., Babin, M., Morel, A. and Claustre, H., (1995). Variability in the chlorophyll-specific absorption coefficients of natural phytoplankton: Analysis and parameterization. Journal of Geophysical Research: Oceans, 100(C7), pp.13321-13332.

[60] Toll, J.S., (1956). Causality and the dispersion relation: logical foundations. Physical review, 104(6), p.1760.

[61] Lain, L.R., Bernard, S. and Evers-King, H., (2014). Biophysical modelling of phytoplankton communities from first principles using two-layered spheres: Equivalent Algal Populations (EAP) model. Optics express, 22(14), pp.16745- 16758.

[62] Lain, L.R. and Bernard, S., (2018). The fundamental contribution of phyto- plankton spectral scattering to ocean colour: implications for satellite detection of phytoplankton community structure. Applied Sciences, 8(12), p.2681.

[63] Behrenfeld, Michael J., Kimberly H. Halsey, and Allen J. Milligan, (2008). Evolved physiological responses of phytoplankton to their integrated growth environment. Philosophical Transactions of the Royal Society B: Biological Sciences, 363.1504: 2687-2703.

[64] Graff, J.R., Westberry, T.K., Milligan, A.J., Brown, M.B., Olmo, G.D., Reifel, K.M. and Behrenfeld, M.J., (2016). Photoacclimation of natural phytoplankton communities. Marine Ecology Progress Series, 542, pp.51-62.

[65] Anning, T., MacIntyre, H. L., Pratt, S. M., Sammes, P. J., Gibb, S. and, R. J., (2000). Photoacclimation in the marine diatom Skeletonema costatum. Limnology and Oceanography, 45(8), pp.1807–1817.

[66] Garcia-Camacho, F., Sanchez-Miron, A., Molina-Grima, E., Camacho-Rubio, F. and Merchuck, J.C., (2012). A mechanistic model of photosynthesis in mi- croalgae including photoacclimation dynamics. Journal of theoretical biology, 304, pp.1-15.

[67] Zonneveld, C., (1998). Photoinhibition as affected by photoacclimation in phytoplankton: a model approach. Journal of Theoretical Biology, 193(1), pp.115- 123.

[68] Lovenduski, N.S. and Gruber, N., (2005). Impact of the Southern Annular Mode on Southern Ocean circulation and biology. Geophysical Research Letters, 32(11).

[69] Moutier, W., Thomalla, S.J., Bernard, S., Wind, G., Ryan-Keogh, T.J. and Smith, M.E., (2019). Evaluation of chlorophyll-a and POC MODIS aqua prod- ucts in the Southern Ocean. Remote Sensing, 11(15), p.1793.

[70] Kishino, M., Takahashi, M., Okami, N. and Ichimura, S., (1985). Estimation of the spectral absorption coefficients of phytoplankton in the sea. Bulletin of marine science, 37(2), pp.634-642.

[71] Stramski, D., Reynolds, R.A., Kaczmarek, S., Uitz, J. and Zheng, G., (2015). Correction of pathlength amplification in the filter-pad technique for mea- surements of particulate absorption coefficient in the visible spectral region. Applied Optics, 54(22), pp.6763-6782.

[72] Series, I.P., (2018). Inherent optical property measurements and protocols:

absorption coefficient. IOCCG ocean optics and biogeochemistry protocols for satellite ocean colour sensor validation, 1.

[73] Wang, S., Ishizaka, J., Hirawake, T., Watanabe, Y., Zhu, Y., Hayashi, M. and Yoo, S., (2015). Remote estimation of phytoplankton size fractions using the spectral shape of light absorption. Optics express, 23(8), pp.10301-10318.

[74] Cleveland, J.S. and Weidemann, A.D., (1993). Quantifying absorption by aquatic particles: A multiple scattering correction for glass-fiber filters. Lim- nology and Oceanography, 38(6), pp.1321-1327.

[75] Sosik, H.M. and Mitchell, B.G., (1995). Light absorption by phytoplankton, photosynthetic pigments and detritus in the California Current System. Deep Sea Research Part I: Oceanographic Research Papers, 42(10), pp.1717-1748.

[76] Roesler, C.S., Perry, M.J. and Carder, K.L., (1989). Modeling in situ phyto- plankton absorption from total absorption spectra in productive inland marine waters. Limnology and Oceanography, 34(8), pp.1510-1523.

[77] Bricaud, A. and Stramski, D., (1990). Spectral absorption coefficients of living phytoplankton and non algal biogenous matter: A comparison between the Peru upwelling area and the Sargasso Sea. Limnology and oceanography, 35(3), pp.562-582.

[78] Neukermans, G., Reynolds, R.A. and Stramski, D., (2016). Optical classification and characterization of marine particle assemblages within the western Arctic Ocean. Limnology and oceanography, 61(4), pp.1472-1494.

[79] Sathyendranath, S, Brewin, RJW, Brockmann, C, Brotas, V, Calton, B, Chuprin, A, Cipollini, P, Couto, AB, Dingle, J, Doerffer, R, Donlon, C, Dowell, M, Farman, A, Grant, M, Groom, S, Horseman, A, Jackson, T, Krasemann, H, Lavender, S, Martinez-Vicente, V, Mazeran, C, Melin, F, Moore, TS, Muller, D, Regner, P, Roy, S, Steele, CJ, Steinmetz, F, Swinton, J, Taberner, M, Thompson, A, Valente, A, Zuhlke, M, Brando, VE, Feng, H, Feldman, G, Franz, BA, Frouin, R, Gould, Jr., RW, Hooker, SB, Kahru, M, Kratzer, S, Mitchell, BG, Muller-Karger, F, Sosik, HM, Voss, KJ, Werdell, J, and Platt, T., (2019). An ocean-colour time series for use in climate studies: the experience of the Ocean-Colour Climate Change Initiative (OC-CCI). Sensors: 19, 4285. doi:10.3390/s19194285.

[80] O Reilly, J.E., Maritorena, S., Siegel, D.A., O Brien, M.C., Toole, D., Mitchell, B.G., Kahru, M., Chavez, F.P., Strutton, P., Cota, G.F. and Hooker, S.B., (2000). Ocean color chlorophyll a algorithms for SeaWiFS, OC2, and OC4: Version 4. SeaWiFS postlaunch calibration and validation analyses, Part, 3, pp.9-23.

[81] Johnson, R., Strutton, P.G., Wright, S.W., McMinn, A. and Meiners, K.M., (2013). Three improved satellite chlorophyll algorithms for the Southern Ocean. Journal of Geophysical Research: Oceans, 118(7), pp.3694-3703.

[82] Lee, Z., Carder, K.L. and Arnone, R.A., (2002). Deriving inherent optical prop- erties from water color: a multiband quasi-analytical algorithm for optically deep waters. Applied optics, 41(27), pp.5755-5772.

[83] Lee, Z., Lubac, B., Werdell, J. and Arnone, R., (2009). An update of the quasi- analytical algorithm (QAA v5). International Ocean Color Group Software Report, pp.1-9.

[84] Ciotti, A.M., Lewis, M.R. and Cullen, J.J., (2002). Assessment of the relation- ships between dominant cell size in natural phytoplankton communities and the spectral shape of the absorption coefficient. Limnology and Oceanography, 47(2), pp.404-417.

[85] Agusti, S., (1991). Light environment within dense algal populations: cell size influences on self-shading. Journal of plankton research, 13(4), pp.863-871.

[86] Z.V. Finkel, A.J. Irwin, O. Schofield., (2004). Resource limitation alters the 3/4 size scaling of metabolic rates in phytoplankton. Marine Ecology-Progress Series, 273, pp. 269-279.

[87] Stramski, D., Rosenberg, G. and Legendre, L., (1993). Photosynthetic and op- tical properties of the marine chlorophyte Dunaliella tertiolecta grown un- der fluctuating light caused by surface-wave focusing. Marine Biology, 115(3), pp.363-372.

[88] L. A. Clementson, J. S. Parslow, A. R. Turnbull, D. C. McKenzie, and C. E. Rathbone., (2001). Optical properties of waters in the australasian sector of the southern ocean, J. Geophys. Res., 106(C12), 31611–31625.

[89] Falkowski, P.G., Chen, YB., (2003). Photoacclimation of Light Harvesting Systems in Eukaryotic Algae. In: Green, B.R., Parson, W.W. (eds) Light- Harvesting Antennas in Photosynthesis. Advances in Photosynthesis and Respiration, 13, pp. 423-447, Springer, Dordrecht.

[90] Zheng, G., Stramski, D. and Reynolds, R.A., (2014). Evaluation of the Quasi- Analytical Algorithm for estimating the inherent optical properties of seawater from ocean color: Comparison of Arctic and lower-latitude waters, also found errors in the partitioning of abs at high latitudes. Remote Sensing of Environ- ment, 155, pp.194-209.

[91] Pitarch, J., Bellacicco, M., Organelli, E., Volpe, G., Colella, S., Vellucci, V. and Marullo, S., (2019). Retrieval of particulate backscattering using field and satellite radiometry: Assessment of the QAA algorithm. Remote Sensing, 12(1), p.77.

[92] Stramski, D. and Mobley, C.D., (1997). Effects of microbial particles on oceanic optics: A database of single-particle optical properties. Limnology and Oceanography, 42(3), pp.538-549.

[93] Stramski, D., (1999). Refractive index of planktonic cells as a measure of cellular carbon and chlorophyll a content. Deep Sea Research Part I: Oceanographic Research Papers, 46(2), pp.335-351.

[94] Graff, Jason R., et al. (2015), Analytical phytoplankton carbon measure- ments spanning diverse ecosystems. Deep Sea Research Part I: Oceanographic Research Papers, 102: 16-25.

[95] Kostadinov, T., Siegel, D., Maritorena, S., (2009). Retrieval of the particle size distribution from satellite ocean color observations. Journal of Geophysical Research: Oceans, 114.

[96] Kostadinov, T.S., Siegel, D.A., Maritorena, S. and Guillocheau, N., (2012). Op- tical assessment of particle size and composition in the Santa Barbara Channel, California. Applied optics, 51(16), pp.3171-3189.

[97] Kostadinov, T.S., Robertson Lain, L., Kong, C.E., Zhang, X., Maritorena, S., Bernard, S., Loisel, H., Jorge, D.S., Kochetkova, E., Roy, S. and Jonsson, B., (2022). Ocean Color Algorithm for the Retrieval of the Particle Size Distribu- tion and Carbon-Based Phytoplankton Size Classes Using a Two-Component Coated-Spheres Backscattering Model. EGUsphere, pp.1-38.

[98] T. J. Ryan-Keogh, E. L. Bone, S. J. Thomalla, L. Lain, M. E. Smith, S. Bernard, M. Vichi. Seasonal drivers of in situ fluorescence quantum yield variability in the Southern Ocean (under review).

[99] T. J. Ryan-Keogh, E. L. Bone, S. J. Thomalla, L. Lain, M. E. Smith, S. Bernard, M. Vichi. Trends in fluorescence quantum yield and the implications for Southern Ocean iron stress (under review).

[100] Bellacicco, M., Pitarch, J., Organelli, E., Martinez-Vicente, V., Volpe, G. and Marullo, S., (2020). Improving the retrieval of carbon-based phytoplankton biomass from Satellite Ocean Colour Observations. Remote Sensing, 12(21), p.3640.

[101] M. J. Behrenfeld, E. Boss, D. A. Siegel, and D. M. Shea, (2005). Carbon-based ocean productivity and phytoplankton physiology from space. Glob. Biogeochem. Cycles 19, 1–14.

[102] Loisel, H., Duforˆet-Gaurier, L., Dessailly, D., Sathyendranath, S., Evers-King, H., Vantrepotte, V., Thomalla, S., Mangin, A. and D'andon, O.H.F., (2018). A satellite view of the particulate organic carbon and its algal and non-algal carbon pools. Ocean Optics XXIV, pp.7-12.

[103] S. Sathyendranath, R. Brewin, T. Jackson, F. M´elin, and T. Platt, (2017). Ocean-colour products for climate-change studies: What are their ideal char- acteristics? Remote Sens. Environ., 203, 125–138.

[104] Dai, Y., Yu, J., Ren, H. and Ji, X., (2022). Deglacial Subantarctic CO2 outgassing driven by a weakened solubility pump. Nature communications, 13(1), pp.1-9.

[105] Lohrenz, S.E., Weidemann, A.D. and Tuel, M., (2003). Phytoplankton spectral absorption as influenced by community size structure and pigment composition. Journal of Plankton Research, 25(1), pp.35-61.

[106] Jackson, T., Sathyendranath, S. and Mélin, F., (2017). An improved optical classification scheme for the Ocean Colour Essential Climate Variable and its applications. Remote Sensing of Environment, 203, pp.152-161.

[107] Martínez-Vicente, V., Evers-King, H., Roy, S., Kostadinov, T.S., Tarran, G.A., Graff, J.R., Brewin, R.J., Dall'Olmo, G., Jackson, T., Hickman, A.E. and Röttgers, R., (2017). Intercomparison of ocean color algorithms for picophytoplankton carbon in the ocean. Frontiers in Marine Science, 4, p.378.

[108] Evers-King, H., Martinez-Vicente, V., Brewin, R.J., Dall'Olmo, G., Hickman, A.E., Jackson, T., Kostadinov, T.S., Krasemann, H., Loisel, H., Röttgers, R. and Roy, S., (2017). Validation and intercomparison of ocean color algorithms for estimating particulate organic carbon in the oceans. Frontiers in Marine Science, p.251.

6. Appendix

6.1. Supplementary Figures

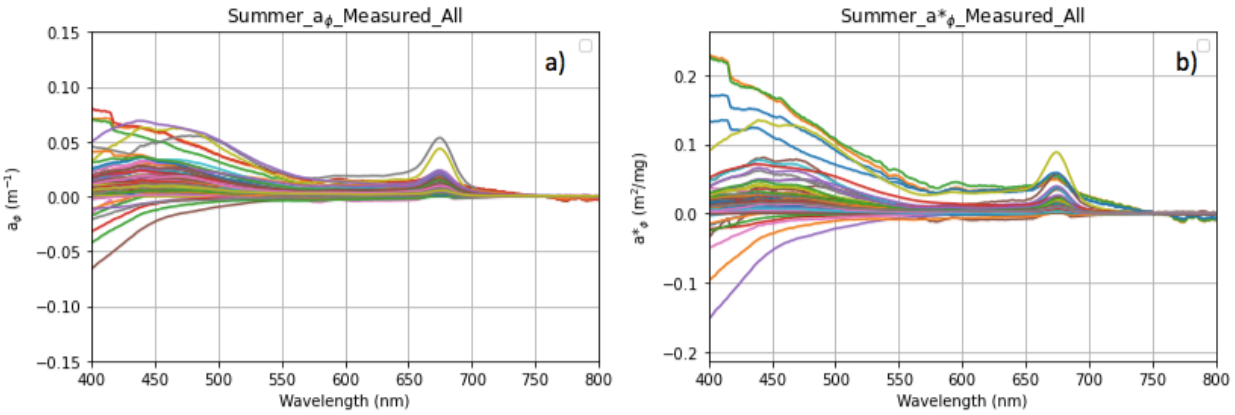

Supplementary Figure S1: Measured a) $a_\Phi(\lambda)$ spectra and b) $a^*_\Phi(\lambda)$ for all stations including the 8 negative spectra that were subsequently removed from the data set.

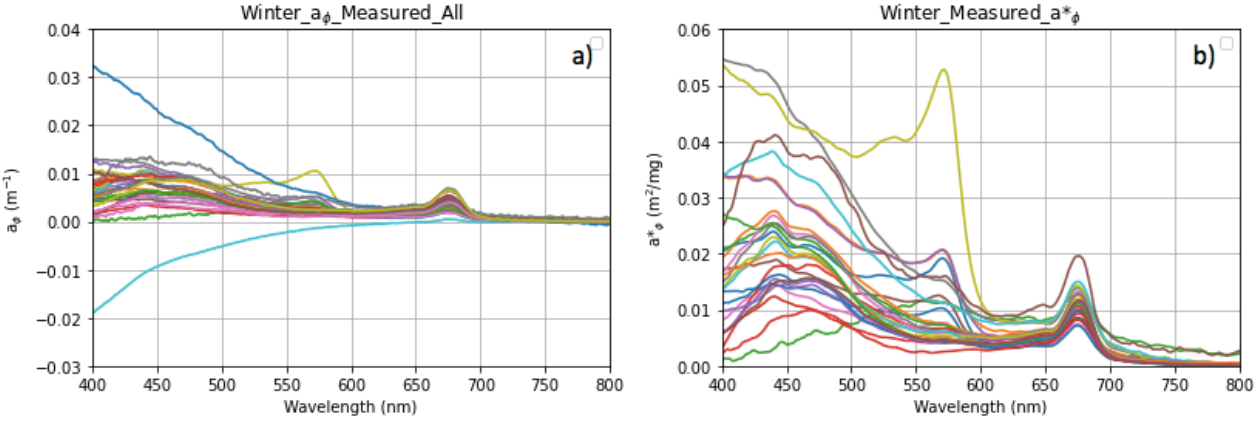

Supplementary Figure S2: Winter: all measured a) $a_\Phi(\lambda)$ spectra b) and $a^*_\Phi(\lambda)$ spectra.

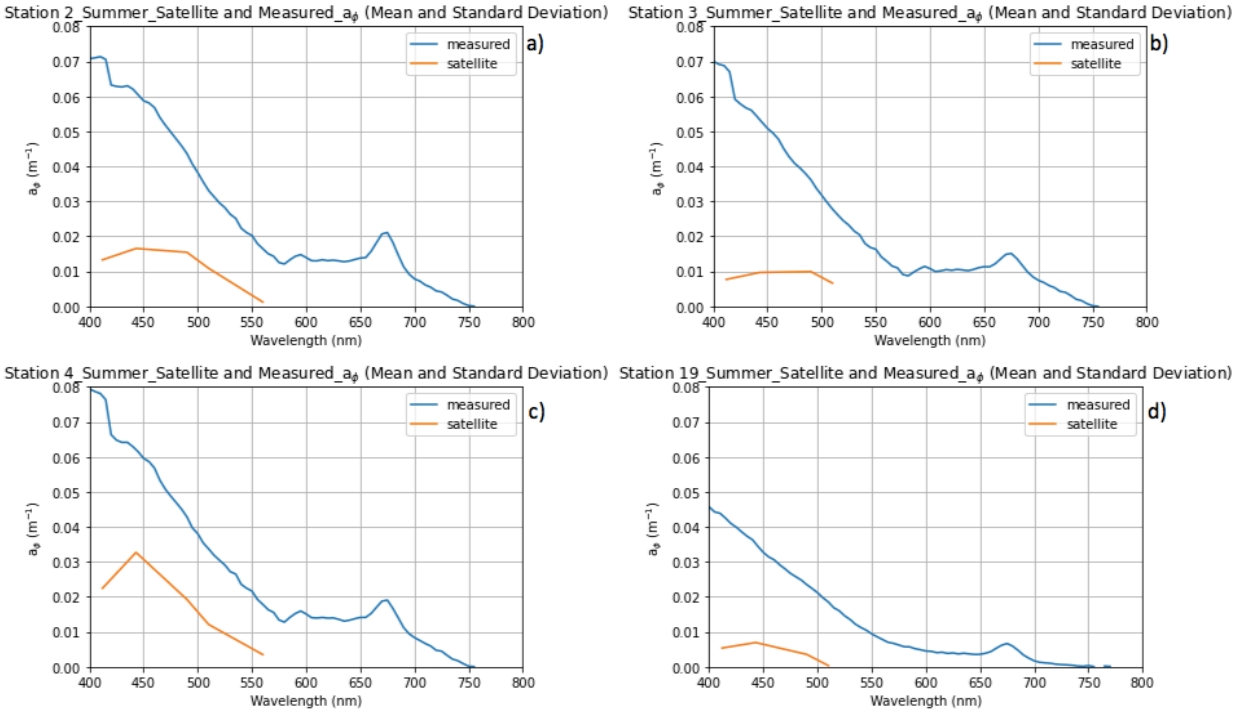

Supplementary Figure S3: Four stations displaying the high $a_{\Phi}(\lambda)$ in the blue wavelength region characteristic of incomplete phytoplankton pigment extraction.

station number	class 1	class 10	class 11	class 12	class 13	class 14	class 2	class 3	class 4	class 5	class 6	class 7	class 8	class 9
1	0,19	0,00	0,00	0,00	0,00	0,00	0,00	0,09	0,06	0,05	0,02	0,85	0,95	NaN
2	0,36	0,97	0,16	0,00	0,00	0,00	0,00	0,00	0,00	0,00	0,00	0,81	0,01	NaN
3	0,15	0,51	0,03	0,00	0,00	0,00	0,00	0,00	0,00	0,00	0,00	0,93	0,14	NaN
4	0,59	0,77	0,05	0,00	0,00	0,00	0,00	0,00	0,00	0,00	0,00	0,76	0,13	NaN
6	0,02	0,10	0,73	0,17	0,00	0,00	0,00	0,00	0,00	0,00	0,00	0,02	0,00	NaN
26	0,79	0,07	0,00	0,00	0,00	0,00	0,00	0,01	0,06	0,12	0,04	0,86	0,95	NaN
27	0,00	0,04	0,02	0,00	0,00	0,00	0,00	0,00	0,00	0,00	0,00	0,99	0,14	NaN
61	0,00	0,84	0,83	0,01	0,00	0,00	0,00	0,00	0,00	0,00	0,00	0,50	0,00	NaN
62	0,00	0,84	0,83	0,01	0,00	0,00	0,00	0,00	0,00	0,00	0,00	0,50	0,00	NaN
63	0,00	0,94	0,17	0,00	0,00	0,00	0,00	0,00	0,00	0,00	0,00	0,95	0,01	NaN

64	*0,00*	*0,98*	*0,27*	*0,00*	*0,00*	*0,00*	*0,00*	*0,00*	*0,00*	*0,00*	*0,00*	*0,91*	*0,00*	*NaN*

Supplementary Figure S4: Membership water class for summer.

station number	*class 1*	*class 10*	*class 11*	*class 12*	*class 13*	*class 14*	*class 2*	*class 3*	*class 4*	*class 5*	*class 6*	*class 7*	*class 8*	*class 9*
3	*0,11*	*0,03*	*0,00*	*0,00*	*0,00*	*0,00*	*0,00*	*0,00*	*0,01*	*0,00*	*0,00*	*0,39*	*0,37*	*NaN*
10	*0,51*	*0,05*	*0,00*	*0,00*	*0,00*	*0,00*	*0,00*	*0,00*	*0,11*	*0,02*	*0,06*	*0,74*	*0,84*	*NaN*
11	*0,00*	*0,60*	*0,10*	*0,00*	*0,00*	*0,00*	*0,00*	*0,00*	*0,00*	*0,00*	*0,00*	*0,99*	*0,04*	*NaN*
12	*0,94*	*0,09*	*0,00*	*0,00*	*0,00*	*0,00*	*0,00*	*0,00*	*0,11*	*0,06*	*0,09*	*0,81*	*0,98*	*NaN*
13	*0,02*	*0,69*	*0,10*	*0,00*	*0,00*	*0,00*	*0,00*	*0,00*	*0,00*	*0,00*	*0,00*	*0,93*	*0,11*	*NaN*
14	*0,08*	*0,03*	*0,00*	*0,00*	*0,00*	*0,00*	*0,00*	*0,03*	*0,08*	*0,01*	*0,01*	*0,95*	*0,95*	*NaN*
15	*0,75*	*0,04*	*0,00*	*0,00*	*0,00*	*0,00*	*0,00*	*0,01*	*0,14*	*0,22*	*0,09*	*0,86*	*0,98*	*NaN*
17	*0,16*	*0,00*	*0,00*	*0,00*	*0,00*	*0,00*	*0,00*	*0,05*	*0,37*	*0,02*	*0,43*	*0,49*	*0,74*	*NaN*
18	*0,16*	*0,00*	*0,00*	*0,00*	*0,00*	*0,00*	*0,00*	*0,08*	*0,37*	*0,13*	*0,50*	*0,65*	*0,89*	*NaN*
21	*0,00*	*0,22*	*0,04*	*0,00*	*0,00*	*0,00*	*0,00*	*0,00*	*0,01*	*0,00*	*0,00*	*0,93*	*0,20*	*NaN*

Supplementary Figure S5: Membership water class for winter.